JCI The Journal of Clinical Investigation

Peroxisomal integrity in demyelination-associated microglia enables cellular debris clearance and myelin renewal in mice

Joseph A. Barnes-Vélez, Xiaohong Zhang, Yaren L. Peña Señeriz, Kiersten A. Scott, Yinglu Guan, Jian Hu

J Clin Invest. 2025. https://doi.org/10.1172/JCI179985.

Research In-Press Preview **Cell biology** **Inflammation** **Neuroscience**

Graphical abstract

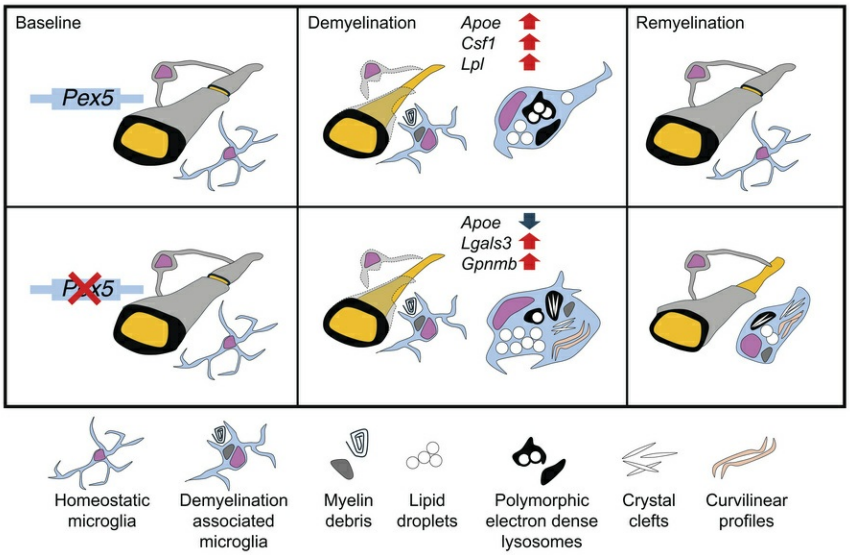

Title Page

Manuscript title

Peroxisomal integrity in demyelination-associated microglia enables cellular debris clearance and myelin renewal in mice

Authors and affiliations

Joseph A. Barnes-Vélez[1,2,3], Xiaohong Zhang[1], Yaren L. Peña Señeriz[4], Kiersten A Scott[2], Yinglu Guan[1], and Jian Hu[1,2,5]

[1]Department of Cancer Biology, MD Anderson Cancer Center, Houston, Texas, USA, 77030; [2]University of Texas MD Anderson Cancer Center UTHealth Graduate School of Biomedical Sciences, Houston, Texas, USA, 77030; [3]University of Puerto Rico School of Medicine, San Juan, Puerto Rico, 00936; [4]University of Puerto Rico at Cayey, Cayey, Puerto Rico, 00736; [5]Cancer Neuroscience Program, MD Anderson Cancer Center, Houston, Texas, USA, 77030

Corresponding author: Jian Hu, 1881 East Rd, South Campus Research Building 3, Houston, Texas, USA, 77030. Phone: 713-794-5238. Email: jhu3@mdanderson.org

Conflict-of-interest statement

The authors have declared that no conflict of interest exists.

Abstract

Demyelination associated microglia (DMAM) orchestrate the regenerative response to demyelination by clearing myelin debris and promoting oligodendrocyte maturation. Peroxisomal metabolism has emerged as a candidate regulator of DMAMs, though the cell-intrinsic contribution in microglia remains undefined. Here we elucidate the role of peroxisome integrity in DMAMs using cuprizone mediated demyelination coupled with conditional knockout of peroxisome biogenesis factor 5 (PEX5) in microglia. Absent demyelination, PEX5 conditional knockout (PEX5cKO) had minimal impact on homeostatic microglia. However, during cuprizone-induced demyelination, the emergence of DMAMs unmasked a critical requirement for peroxisome integrity. At peak demyelination, PEX5cKO DMAMs exhibited increased lipid droplet burden and reduced lipophagy suggestive of impaired lipid catabolism. Although lipid droplet burden declined during the remyelination phase, PEX5cKO DMAMs accumulated intralysosomal crystals and curvilinear profiles, which features were largely absent in controls. Aberrant lipid processing was accompanied by elevated lysosomal damage markers and downregulation of the lipid exporter gene *Apoe*, consistent with defective lipid clearance. Furthermore, the disruptions in PEX5cKO DMAMs were associated with defective myelin debris clearance and impaired remyelination. Together, these findings delineate a stage-specific role for peroxisomes in coordinating lipid processing pathways essential to DMAM function and necessary for enabling a pro-remyelinating environment.

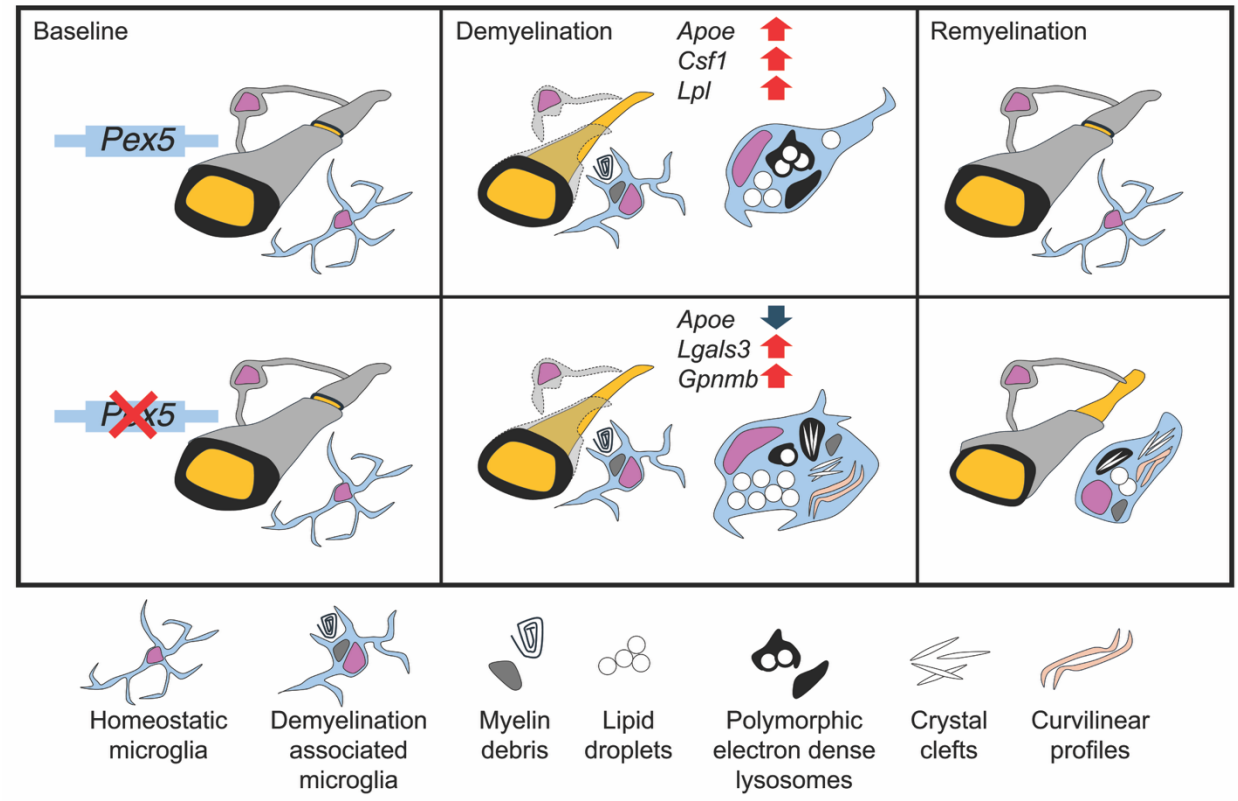

40

41 Loss of peroxisomal integrity disrupts myelin debris-derived lipid processing in demyelination

42 associated microglia and undermines myelin debris clearance and remyelination.

43

Main Text

Introduction

Peroxisomes are single membrane bound organelles required for a subset of metabolic pathways, including ether lipid synthesis and very long chain fatty acid oxidation (1). Recently, evidence linking peroxisomes to immunometabolism (2) has been described in macrophages, wherein through cell intrinsic mechanisms peroxisomes facilitate pathogen clearance (3), cytokine release (4), and bioactive lipid precursor mobilization (5). Moreover, peroxisomal lipid oxidation regulates adaptations to age-related stress in microglia, the predominant subset of brain resident macrophages (6, 7). Microglia drive a critical response to demyelination by clearing myelin debris and enabling newly formed oligodendrocytes to remyelinate denuded axons (8). Studies in peroxisomal disease have suggested that peroxisomes also contribute to DMAMs and the microglial response in demyelination. For instance, in adrenoleukodystrophy, germline mutations disrupting peroxisomal lipid oxidation can precipitate demyelination associated with perilesional microglial stress and loss (9, 10). However, whether peroxisomes facilitate DMAMs cell autonomously and to what extent remain unclear.

To ascertain the cell intrinsic role of peroxisomes in DMAMs, we disrupted peroxisome biogenesis in microglia by conditional depletion of PEX5 (encoded by *Pex5*) within the context of cuprizone induced demyelination. PEX5 loss redirected microglial activation into DMAMs enriched for lysosome damage related genes *Lgals3* and *Gpnmb*. In contrast to peroxisome intact DMAMs, lipid droplet clearance in PEX5cKO DMAMs correlated with notable crystal accumulation and loss of lipophagy-invoking structures. Moreover, PEX5 depletion in DMAMs reduced myelin debris clearance and pro-remyelination factor expression which correlated with

impaired remyelination. In summary, the microglial response during demyelination is intrinsically dependent on peroxisomal integrity for acquiring a pro-remyelinating phenotype.

Results

Validation of PEX5 depletion in myeloid cells

We asked whether microglia intrinsically depend on peroxisomes to facilitate a response to demyelination. To address this question, we achieved PEX5cKO using *Cx3cr1*$^{CreERT2/wt}$, *Pex5*$^{lox/lox}$ mice (11, 12), in which tamoxifen-inducible Cre recombinase drives PEX5 depletion in myeloid cells, including microglia. *Cx3Cr1*$^{CreERT2/wt}$, *Pex5*$^{lox/wt,\ wt/wt}$ littermates served as controls. In vitro, 4-hydroxytamoxifen exposure downregulated both *Pex5* mRNA and PEX5 protein in PEX5cKO bone marrow-derived macrophages relative to control (Supplemental Figure 1 A, B, C). Since PEX5 loss undermines peroxisome biogenesis (13), we examined peroxisome integrity. Immunolabeling for peroxisome membrane protein 70 (PMP70) revealed that PEX5cKO macrophages, relative to control, exhibited fewer and larger PMP70^{+} punctae, suggestive of enlarged ghost peroxisomes or peroxisomal clumping (Supplemental Figure 1D,E,F) indicative of disrupted peroxisome homeostasis (13).

Experimental design to assess the role of PEX5 in DMAMs

To evaluate the effects of PEX5 loss in DMAMs, we fed adult PEX5cKO and control littermates 0.2% cuprizone diet for 6 weeks (Supplemental Figure 1G). Two weeks prior to starting cuprizone, both PEX5cKO and control littermates received tamoxifen (2 mg daily, five consecutive days) to induce PEX5 knockout and enable turnover of healthy peroxisomes to dysfunctional peroxisomes (14). After six weeks with cuprizone, brain samples were collected to assess peak demyelination (CPZ). Baseline condition consisted of PEX5cKO and control littermates kept on standard chow

throughout the study (Supplemental Figure 1G). Whole brain samples were collected and submitted to single nuclei RNA sequencing for transcriptional profiling of the cell types of interest.

PEX5 loss diverges DMAM evolution following demyelination

Following quality control, dimensionality reduction, cell clustering, and cell marker-based annotation (Supplemental Figure 2A, B, C; Supplemental Table 1), we detected 29 cell clusters, 24 of which were neuronal (*Syt1* enriched) and further categorized into glutamatergic (*Slc17a7*, *Slc17a6* expressing) and GABAergic (*Gad1*, *Gad2* expressing) subtypes (Figure 1A, B; Supplemental Figure 2C). Non-neuronal clusters included oligodendrocytes, immune cells, oligodendrocyte progenitor cells (OPC), astrocytes, and vascular leptomeningeal cells (VLMC) (Figure 1A; Supplemental Figure 2C). CPZ samples exhibited oligodendrocyte loss alongside increased immune cell and OPC counts relative to baseline (Figure 1B), which findings were consistent with oligodendrocyte cell death, inflammation, and increased remyelination-mediating OPCs expected with cuprizone exposure (15).

As PEX5 loss was targeted to myeloid cells and microglia, we performed immune cell sub-analysis. Among immune cells, we detected 9 subclusters, of which 7 were comprised of microglia, characterized by *Hexb* and *Tgfbr1* enrichment (Figure 1C, D, E; Supplemental Table 2). The remaining two non-microglial clusters included macrophages (*Mrc1*, *F13a1* expressing) and lymphocytes (*Skap1*, *Itk* expressing) (Figure 1E). Under baseline conditions, the bulk of microglia expressed homeostatic genes *P2ry12* and *Cx3cr1* (16) (Figure 1C, E, F).

Within the CPZ arm, microglia underwent a marked shift in cell states. Microglia exhibiting intermediate expression of activation-related genes (*Axl*, *Apoe*) were labeled as Intermediate microglia (Figure 1E). Microglia that strongly upregulated activation-related genes and downregulated homeostatic genes were classified as DMAMs and were subclassified into 3

clusters labeled as DMAM0, DMAM1, and DMAM2 (Figure 1E). Relative to DMAM0, the DMAM1 and DMAM2 clusters acquired additional markers beyond hallmark activation genes. Among marker genes, DMAM1 exhibited high expression of *Lpl* and *Csf1* and intermediate expression of *Lgals3*, whereas DMAM2 demonstrated high expression of *Lgals3* and high expression for *Gpnmb* (Figure 1C, E). Consistent with an inflammatory response, we also identified proliferating microglia (Cycling) and interferon responsive microglia (IRM) enriched for interferon pathway genes (Figure 1E).

Notably, the DMAM2 cluster was almost exclusively identified in PEX5cKO samples within the CPZ arm, whereas control DMAMs predominantly consisted of DMAM0 and DMAM1 clusters (Figure 1F). Fold change analysis confirmed a significant increase in the DMAM2 cell fraction in PEX5cKO CPZ samples, accompanied by a reduction in DMAM0 and DMAM1 cell fractions relative to control CPZ samples (Figure 1G). We next performed pseudotime analysis to elucidate the developmental trajectory of the DMAM clusters (17). Selecting homeostatic microglia as the origin cluster, pseudotime analysis revealed a sequential developmental trajectory of homeostatic microglia into Intermediate and DMAM0 microglia (Figure 1H). From DMAM0 state, activated microglia then diverged into DMAM1 or DMAM2 states (Figure 1H, I, J). Coupling pseudotime and fold change analyses indicated that PEX5cKO reprogrammed the DMAM evolution, redirecting DMAMs away from the DMAM1 state and towards the PEX5cKO-enriched DMAM2 state.

PEX5cKO undermines *Apoe* expression in activated microglia

To identify molecular changes driving the altered DMAM states downstream of PEX5 depletion, we performed pseudobulk analysis comparing control and PEX5cKO genotypes across the immune clusters within the CPZ arm. Using an adjusted p value cutoff of 0.15, we identified

relatively few differentially expressed genes (DEGs) across the subclusters (Figure 2A; Supplemental Table 3). No DEGs were identified in the DMAM2 cluster, likely because the cluster was predominantly comprised of PEX5cKO cells (Figure 2A). However, triangulation of downregulated DEGs revealed that *Apoe* expression was decreased in PEX5cKO samples across the DMAM0, DMAM1, and Intermediate clusters (Figure 2B). The *Apoe* gene encodes for apolipoprotein E (APOE), a critical activation-related protein. *Apoe* expression is strongly induced in DMAMs following demyelination, as was observed in our single nuclei RNA sequencing data (Figure 2C), which demonstrated both increased average as well as higher percent expression of *Apoe* in Intermediate and DMAM clusters relative to homeostatic microglia. However, *Apoe* expression in the Intermediate and DMAM clusters was significantly impaired in PEX5cKO samples (Figure 2D). Thus, *Apoe* expression in the context of cuprizone-induced demyelination is dependent on PEX5 and presumably peroxisome integrity in microglia.

Impaired *Apoe* expression correlates with exacerbated lipid droplet accumulation and crystal precipitation in PEX5cKO tissue

Following cell debris uptake, DMAMs upregulate lipid droplet biogenesis and *Apoe* dependent lipid export (18). *Apoe* downregulation and impaired lipid export undermine the pro-remyelinating properties and exacerbate lipid droplet burden in microglia (19). To assess for lipid droplets, we performed transmission electron microscopy (TEM) to quantitate lipid droplets within lesion-associated phagocytes. Additionally, to assess the impact of PEX5 depletion on remyelination, a third experimental arm was added, wherein after six weeks of cuprizone diet, PEX5cKO and control littermates were switched back to standard chow for ten days (postCPZ) (Supplemental Figure 1G).

Using TEM, lipid droplets were visualized in CPZ and postCPZ conditions relative to baseline, consistent with the expected increase in lipid droplet biogenesis in DMAMs during demyelination (Figure 2E, F, G). In agreement with impaired *Apoe* gene expression, we observed that lipid droplet counts per phagocyte were elevated in PEX5cKO relative to control at both the CPZ and postCPZ conditions (Figure 2E, F, G). Lipid droplet burden peaked in the CPZ arm and declined in the postCPZ arm for both PEX5cKO and control, indicative that although PEX5 loss exacerbated lipid droplet burden, lipid droplet clearance remained intact (Figure 2E, F, G).

Lipid droplet processing requires the export of cholesterol via lipoproteins, including APOE (20). Control DMAMs expressing APOE are expected to more effectively extrude lipids via lipoprotein-dependent mechanisms. *Apoe* downregulation in PEX5cKO DMAMs suggest that the resolution of lipid droplets was associated with defective lipid export. Impaired lipid export following lipid droplet catabolism can lead to aberrant accumulation of lipids in other subcellular structures, including lipid crystals (19). Elevated intracellular sterol concentration secondary to APOE loss in myelin debris clearing microglia is associated with sterol crystal precipitation (19). Accordingly, we observed a marked increase in crystal clefts within PEX5cKO phagocytes (Figure 2H, I). Both frequency of crystal positive phagocytes and per cell crystal burden peaked in PEX5cKO postCPZ samples, following an inverse trend relative to lipid droplet burden (Figure 2H, I). In contrast, crystals were less frequently observed in control samples during demyelination and remained undetected within control postCPZ samples (Figure 2H, I). Therefore, unlike in control, lipid droplet resolution in PEX5cKO samples was directly associated with crystal accumulation.

Consistent with the TEM analysis, lipid droplets were readily detected in lectin^{+} phagocytes following demyelination using BODIPY dye (Figure 2J). Although BODIPY^{+} cell

counts resolved in the postCPZ arm across genotypes (Figure 2K), BODIPY$^+$ punctae remained increased in PEX5cKO lectin$^+$ phagocytes relative to control (Figure 2L), thus validating our TEM assessment that PEX5 loss exacerbated lipid droplet burden without blocking lipid droplet resolution. Crystals in tissue can be detected as reflective particles using reflection microscopy. Accordingly, dual confocal and reflection microscopy detected microclusters of reflective particles within lectin$^+$ phagocytes at both the CPZ and postCPZ conditions (Figure 2M, N). Importantly, the average area for reflective particle microclusters was significantly higher in PEX5cKO lectin$^+$ phagocytes relative to control and increased in the postCPZ relative to CPZ conditions, suggestive of higher crystal burden in PEX5cKO postCPZ samples following lipid droplet resolution (Figure 2M, N). Thus, our tissue staining, reflective microscopy, and electron microscopy data are consistent with impaired lipid processing in PEX5cKO DMAMs.

In summary, control samples exhibited an expected pattern of lipid droplet biogenesis and resolution within CPZ and postCPZ conditions. In contrast, PEX5cKO DMAMs exhibited an exacerbated burden of lipid droplets and accumulation of intracellular crystals correlating with lipid droplet resolution.

Impaired lipophagy in PEX5cKO correlates with intralysosomal crystals and curvilinear profiles

Lipid droplets are processed in part by lipophagy, which enables autophagy mediated lipid catabolism through fusion of lipid droplets with lysosomes (21, 22). In control samples following cuprizone mediated demyelination, large (0.75 μm^2 and 1.08 μm^2 median areas in CPZ and postCPZ arms, respectively), polymorphic, electron-dense lysosomes (PEDLs) were observed fusing with lipid droplets within phagocytes, suggestive of lipophagy (Figure 3A). The frequency

and intracellular count of PEDLs peaked during demyelination and correlated with the peak lipid droplet density described above (Figure 3B, C).

Interestingly, relative to control, PEDLs were scarcer in PEX5cKO phagocytes (Figure 3B, C) and presented with smaller areas (0.65 μm^2 and 0.51 μm^2 median areas in CPZ and postCPZ, respectively) (Figure 3D). Moreover, PEX5cKO phagocytes exhibited a higher incidence of crystal clefts within PEDLs (Figure 3E), suggestive of impaired lipid extraction from lysosomes, leading to lipid accumulation and crystal precipitation. Thus, loss of PEX5 and peroxisome integrity present with findings suggestive of impaired intracellular lipid processing following debris engulfment, including lipophagy disruption and accumulation of intralysosomal crystals.

Additional to intralysosomal crystal accumulation, we observed the formation of hypodense, curvilinear profiles within PEX5cKO phagocytes during and after cuprizone exposure (Figure 3F), with more than 50% of PEX5cKO phagocytes in the postCPZ condition presenting with the same (Figure 3G). Pathology reports described the occurrence of laminar profiles in brain phagocytes in cases with adrenoleukodystrophy that were hypothesized to consist of lipid deposits with very long chain fatty acids (23, 24). The enrichment of curvilinear profiles in PEX5cKO phagocytes therefore raises the possibility of a convergence in pathologies between brain phagocytes in cuprizone-fed PEX5cKO mice and adrenoleukodystrophy.

PEX5cKO DMAMs exhibit exacerbated GAL3 response and lysosome turnover

Intralysosomal crystals can compromise lysosome integrity and induce cell stress (19). Accordingly, PEX5cKO samples exhibited a significantly higher number of cycling microglia (Figure 1G), suggestive of higher microglial turnover secondary to cell death from lysosome injury. Additionally, single nuclei RNA sequencing revealed an increase in *Lgals3* expression in DMAM2 state enriched in PEX5cKO samples (Figure 1E). *Lgals3* encodes for galectin 3 (GAL3),

a glycoprotein-binding factor involved in lysosome damage response (25, 26). Whereas *Lgals3* was near undetectable in homeostatic and Intermediate microglial clusters, *Lgals3* achieved low expression in DMAM0 and IRM clusters, and intermediate and high expression in DMAM1 and DMAM2 clusters, respectively (Figure 1E). The expression pattern for *Lgals3* is consistent with previous reports describing GAL3 upregulation in activated but not resting microglia (27). Consistent with the paucity of DMAMs at baseline condition, immunofluorescence analysis demonstrated that $GAL3^+$ cells were nearly undetectable in both control and PEX5cKO baseline samples (Figure 4A, B). In the CPZ arm, $GAL3^+$ cell counts significantly increased, reflecting the emergence of DMAMs during demyelination. In the postCPZ arm, $GAL3^+$ cell counts dropped, consistent with a resolution in demyelination (Figure 4A, B). Overall, $GAL3^+$ staining correlated with the expected dynamics for DMAM cell counts associated with cuprizone use.

$GAL3^+$ cell counts did not substantially differ between PEX5cKO and control under CPZ and postCPZ conditions (Figure 4B). However, in agreement with the transcriptomic analysis, PEX5 depletion increased GAL3 staining intensity per cell relative to control following cuprizone mediated demyelination (Figure 4C). Thus, PEX5 knockout promoted a shift favoring GAL3-high expressing DMAMs, congruent with the enrichment of *Lgals3*-high expressing DMAM2 cluster in PEX5cKO samples.

Additional to increased GAL3 expression, PEX5cKO DMAMs also exhibited greater formation of intracellular $GAL3^+$ punctae that frequently co-labeled with lysosomal associated membrane protein 1 (LAMP1) (Figure 4D, E). Following lysosome injury, GAL3 localizes to the exposed lysosomal lumen enabling a signaling cascade driving lysosome repair and turnover (28). GAL3 upregulation and robust formation of $GAL3^+$ punctae in PEX5cKO DMAMs suggested an intact response to lysosome injury expected with intralysosomal crystals detected with TEM.

Accordingly, using DEG and pathway enrichment analyses between clusters, we observed that relative to both DMAM1 and DMAM0, the DMAM2 cluster was significantly enriched for the lysosome gene pathway, compatible with elevated lysosome turnover secondary to injury and expected with an activated, GAL3-dependent injury response. (Figure 4F, G; Supplemental Table 4).

All together transcriptomic and imaging data indicate that PEX5 knockout and loss of peroxisome integrity undermine lysosome mediated degradation of lipids traceable through intralysosomal crystals, GAL3 upregulation and redistribution, and increased lysosome turnover.

Myelin debris uptake in PEX5cKO macrophages can partially reproduce the DMAM2 cluster-associated signature

Our data indicate that DMAMs responding to demyelination depend on PEX5 for mitigating crystal accumulation. A primary function of DMAMs includes myelin debris clearance. To assess whether perturbations in PEX5cKO DMAMs were unmasked by myelin debris uptake, we asked whether challenging PEX5cKO macrophages with myelin debris could replicate DMAM2 cluster-associated signatures.

We generated bone marrow-derived macrophages from control and PEX5cKO littermates. In all conditions, culture medium was supplemented with 4-hydroxytamoxifen to enable PEX5 depletion. Macrophages were supplemented with purified myelin debris for 24 (24h) and 72 hours (72h) and collected for bulk RNA sequencing. Myelin debris naïve macrophages (resting) served as baseline references (Supplemental Figure 3A).

Principal component and DEG analyses demonstrated that PEX5 knockout had a subdued impact under baseline conditions, with minimal separation between resting macrophage transcriptomes (Supplemental Figure 3B), consistent with our findings in vivo where PEX5cKO

and control homeostatic microglia remained comparable. Next, following myelin debris engulfment, macrophage transcriptomes diverged significantly between PEX5cKO and control genotypes (Supplemental Figure 3B), with DEGs rising to 244 at 24 hours, and further climbing to 1115 following 72 hours of myelin debris exposure (Supplemental Figure 3C, D; Supplemental Table 5). The higher DEG count in bone marrow-derived macrophages relative to DMAMs likely reflected a higher sensitivity to transcriptomic changes afforded by deeper bulk sequencing relative to single nuclei RNA sequencing, inherent differences between bone marrow-derived macrophages and microglia and between in vitro and in vivo conditions. However, 16 of 87 DEGs upregulated in the DMAM2 cluster relative to DMAM1 were also upregulated in PEX5cKO macrophages relative to control after 72 hours of myelin exposure (Supplemental Figure 3E). Importantly, the shared DEGs included *Gpnmb* and *Lgals3* (Supplemental Figure 3E, F). Additionally, pathway enrichment analysis exhibited enrichment for lysosome pathways in PEX5cKO macrophages relative to control across both timepoints of myelin debris exposure, as had been seen with DMAM2 (Supplemental Figure 3G). Interestingly, *Apoe* expression was not affected by PEX5 status in bone marrow-derived macrophages, either at baseline or following myelin debris exposure, indicative that reliance of *Apoe* expression on PEX5 remains context or cell type dependent (Supplemental Figure 3F). However, Ingenuity pathway upstream regulator activity analysis inferred impaired APOE activity at both timepoints of myelin debris exposure (Supplemental Figure 3H), indicative that although *Apoe* expression remained intact in PEX5cKO macrophages, APOE related pathways were deficient, including reduced expression of *Abca1* (Supplemental Figure 3F). Finally, gene set enrichment analysis of transcriptional signatures derived from published single cell RNA sequencing datasets demonstrated that foamy microglia signatures were enriched in PEX5cKO macrophages relative to control post myelin debris uptake

(Supplemental Figure 3I; Supplemental Table 6), consistent with the exacerbated lipid laden phenotype we observed in vivo in PEX5cKO DMAMs.

In summary, myelin debris uptake in PEX5cKO bone marrow-derived macrophages can partially reproduce the molecular signature associated the DMAM2 cluster, indicative that myelin debris uptake in PEX5cKO phagocytes is a contributing factor to DMAM2 cluster emergence.

Emergence of DMAM2 cluster in PEX5cKO samples correlates with impaired remyelination

To assess the impact of DMAM disruption on remyelination, we analyzed the oligodendroglia lineage within the single nuclei RNA sequencing dataset. Our dataset included OPCs and 9 subclusters of *Mbp*$^{+}$ oligodendrocytes (Supplemental Figure 4A, C; Supplemental Table 7). Cell marker annotation elucidated committed oligodendrocyte progenitors and newly formed oligodendrocytes (COP/NFOL) notable for *Frm4da* and *Tcf7l2* enrichment (Supplemental Figure 4A, C), myelin-forming oligodendrocytes (MFOL) which upregulated *Man1a* and *Synpr* and myelin genes including *Mog* and *Mobp* (Supplemental Figure 4A, C), and mature oligodendrocytes (MOL), which downregulated immature marker *Pcdh7* and upregulated MOL subtype 5/6 (MOL5/6) associated genes *Il33* and *Ptgds* or MOL subtype 2 (MOL2) associated gene *Anln* (Supplemental Figure 4A, C). We also detected two additional variations of MOL5/6 notable for enrichment of *Adgrv1* (*Adgrv1*$^{+}$ MOL5/6) and *Clca4a* (*Clca4a*$^{+}$ MOL5/6).

In the CPZ arm, we observed the emergence of a demyelination associated oligodendrocyte (DOL) cluster, notable for enrichment for *Tenm4* expression and only weak expression of MOL5/6 and MOL2 markers (Supplemental Figure 4A, C). Two additional clusters emerged, including *Sox6*-high DOLs (*Sox6*$^{+}$ DOL) and interferon responsive oligodendrocytes (IRO) with interferon pathway gene upregulation (Supplemental Figure 4A, C). Interestingly, pseudotime analysis indicated that DOLs emerged from MFOLs in the context of cuprizone exposure, suggesting that

continual exposure to cuprizone shifts MFOLs from the MOL lineage and towards the DOL state (Supplemental Figure 4F).

PEX5cKO status did not significantly affect cell cluster fractions when assessing fold change relative to control (Supplemental Figure 4B, D, E), moreover, pseudobulk analysis between PEX5cKO and control across clusters revealed relatively few DEGs (Supplemental Table 8). Interestingly, DOLs demonstrated a marked upregulation of *Apod* gene expression, (Supplemental Figure 4G, H, I) which is associated with oligodendrocyte stress response during ischemia (29, 30), suggestive for an elevated stress-promoting environment secondary to PEX5 knockout in DMAMs.

Immunofluorescence analysis demonstrated that $SOX10^+$, $ASPA^+$ oligodendrocyte cell counts and $PDGFR\alpha^+$ OPCs remained comparable between PEX5cKO and control across baseline, CPZ, and postCPZ conditions (Figure 5). However, we detected reduced myelin basic protein (MBP) staining in PEX5cKO samples relative to control (Figure 6A, B) at the CPZ and postCPZ conditions. The MBP deficit between PEX5cKO and control indicated a disruption in remyelination, which begins by six weeks of cuprizone diet (15). TEM analysis validated a reduction in myelinated axon counts in PEX5cKO relative to control, most prominently in the postCPZ arm (Figure 6C, D). Likewise, within the postCPZ condition, we observed an elevated myelin g-ratio in PEX5cKO samples relative to control, consistent with impaired remyelination (Figure 6E, F). Furthermore, we observed an aggravated burden of injured axons detectable as deposits of synaptophysin (SYP) in the corpus callosum of PEX5cKO animals relative to control during remyelination, indicative of a higher incidence of axon damage associated with impaired remyelination (Supplemental Figure 4J, K) (31).

Impaired myelin debris clearance or loss of pro-remyelination factors provided by microglia can undermine remyelination (8). Accordingly, within DMAMs we observed a marked accumulation of degraded myelin basic protein (dMBP), a marker for myelin debris, suggestive of a disruption in myelin debris clearance (Figure 6G, H). Additionally, we observed a decrease in pro-remyelinating factor *Igf1* expression in PEX5cKO DMAMs relative to control (Figure 6I).

In summary, we report that loss of PEX5 and peroxisome integrity in DMAMs profoundly disrupts DMAM homeostasis with adverse consequences reflected in impaired remyelination driven in part by loss of pro-remyelinating factors and impaired myelin debris clearance.

Discussion

Peroxisomes facilitate immunity-related tasks including interferon expression (32), cytokine release, and pathogen clearance in macrophages (2-4). The present study demonstrates that peroxisomes also harbor a cell-intrinsic role in microglia critical to remyelination. Key findings indicate that impaired peroxisome biogenesis redirected the microglial response during demyelination, expanding a pool of crystal-laden DMAMs deficient in debris clearance and associated with impaired remyelination, lysosome injury markers, and downregulation of the critical sterol-exporter gene *Apoe*.

Using single nuclei RNA sequencing, marker gene expression coupled with pseudotime analysis revealed that cuprizone-mediated demyelination robustly recruited DMAMs, a subset of which acquired a lipid-laden phenotype as indicated by lipid staining and transmission electron microscopy. PEX5 knockout did not abate the formation of DMAMs but rather expanded an alternative DMAM state notable for lysosome gene set enrichment, lysosome damage-related genes *Lgals3* and *Gpnmb*, and exacerbated lipid droplet and crystal burden. *Gpnmb* and *Lgals3* expression is associated with lysosome stress and damage, including within microglia (33, 34). A

recent preprint associated GPNMB (gene product for the *Gpnmb* human ortholog)-enriched foamy microglia with poorer outcomes in Multiple Sclerosis patients, implicating GPNMB as a potential marker for lesion exacerbating foamy microglia in Multiple Sclerosis (34). Conversely, the *Lgals3* gene product, GAL3, is lysosome damage response protein, localizing to the exposed lumen of injured lysosomes to help mediate lysosome repair and turnover (25, 26). Our findings align with the above reports, revealing that *Lgals3* and *Gpnmb* expression correlate with lipid-laden microglia that exhibit features of lysosome stress, namely intralysosomal crystals and increased lysosome turnover, and with defective remyelination and exacerbated axonal injury. Importantly, our findings indicate that one pathomechanism leading to lysosome-stressed, foamy microglia includes defective peroxisome biogenesis.

How disruption of peroxisome biogenesis contributes to lipid crystal accumulation remains undefined, however, *Apoe* gene downregulation suggests that impaired sterol export could contribute to lipid saturation and crystal precipitation in PEX5cKO DMAMs. *Apoe* gene encodes for APOE, which is robustly induced in activated microglia (35). APOE knockout mice have frequently been used as a model for atherosclerosis, giving rise to foamy cells laden with cholesterol crystals (19, 36). Importantly, APOE loss in microglia exacerbates cholesterol crystal precipitation during demyelination and impairs remyelination (19). Sterol export pathway gene products, including APOE, are transcriptionally regulated in part by liver X receptor (LXR), a nuclear receptor activated by oxysterols and sterol intermediates (37). During demyelination, DMAMs repurpose *de novo* sterol synthesis to upregulate desmosterol, which activates LXR and upregulates sterol exporter genes *Abca1* and *Apoe*, facilitating lipid export and protecting against crystal precipitation (38). PEX5 regulates peroxisome biogenesis through post-translational mechanisms, mainly by translocating matrix proteins into peroxisomes (39), making direct

384 transcriptional regulation a less plausible mechanism by which PEX5 could affect *Apoe*
385 expression. However, peroxisomes have long been associated with sterol synthesis and are
386 reported to house various sterol synthesizing enzymes, including enzymes upstream of
387 desmosterol (40, 41). Therefore, PEX5 knockout could indirectly affect *Apoe* expression by
388 undermining peroxisome-dependent synthesis of LXR-activating sterol intermediates. However,
389 the extent and context of peroxisome contribution to sterol synthesis remains debated (42, 43).
390 An alternative mechanism relating impaired peroxisome integrity to crystal accumulation
391 stems from our TEM findings. In contrast to PEX5cKO phagocytes, PEX5 intact phagocytes
392 harbored large (frequently exceeding 1.0 μm in diameter), PEDLs fused with lipid droplets,
393 structures evocative of lipophagy (21, 22). Moreover, the prevalence for PEDLs correlated with
394 lipid-laden DMAMs during peak demyelination and resolved with lipid droplet clearance
395 following cuprizone removal. PEX5cKO DMAMs exhibited fewer and smaller PEDLs, a higher
396 fraction of which were crystal laden. Moreover, the lower number of PEDLs in PEX5cKO
397 DMAMs correlated with a higher density of lipid droplets, suggesting an impaired lipophagy, a
398 critical process in lipid droplet clearance that crosstalks with lipolysis (21, 22). Peroxisomes are
399 reported to facilitate intracellular cholesterol trafficking between lysosomes and extra-lysosomal
400 compartments (44). Loss of peroxisome biogenesis factors disrupted sterol export leading to
401 intracellular sterol accumulation (44). Plausibly, PEX5 depletion in DMAMs undermines the
402 ability for peroxisomes to extract sterols from lysosomes, contributing to intra-lysosomal sterol
403 saturation and crystal formation (45). Conversely, peroxisomes can integrate into multi-organelle
404 units in activated macrophages, wherein peroxisomes facilitated the lipolysis of lipid droplets and
405 release of inflammatory fatty acids in a PEX5 dependent manner (5). Interestingly, PEX5 has been
406 implicated in starvation-related lipolysis by facilitating the translocation of adipose triglyceride

lipase to lipid droplets (46). Therefore, peroxisome integrity may affect lipophagy by regulating lipid trafficking from lysosomes or through lipophagy-lipolysis crosstalk (22).

Myelin debris can impede remyelination by preventing maturation of newly formed oligodendrocytes (47, 48). Moreover, maturation of remyelinating oligodendrocytes relies on pro-remyelinating factors produced by DMAMs, including insulin like growth factor (encoded by *Igf1*) (8, 49). Our data revealed both a deficit in myelin debris clearance as well reduced expression of *Igf1* gene, indicating that PEX5cKO DMAMs were less efficient in providing a pro-remyelinating environment relative to their PEX5 intact counterparts. In macrophages, peroxisomes enable uptake and clearance of pathogens (3, 50). Interestingly, PEX5cKO DMAMs accumulated myelin debris relative to control, suggesting a delay in myelin debris degradation following internalization. Lipid dysregulation and accumulation disrupts lysosome function (51, 52), and lysosome dysfunction in turn impairs myelin debris clearance (53, 54). Therefore, defective lipid droplet clearance and elevated lipid and crystal burden in lysosomes could adversely interact with myelin debris degradation within lysosomes, although it remains plausible that peroxisomes affect degradation of endo-lysosomal cargo independent of lipid droplet clearing mechanisms, including via generation of radical nitrogen and oxygen species (3).

Our data indicate that peroxisomes are integral to DMAMs and may offer insights to peroxisomal disorders characterized by disruptions in microglia. Microglial dysfunction features prominently in adrenoleukodystrophy, a peroxisomal disorder driven by mutations to ATP-binding cassette subfamily D member 1 (encoded by *ABCD1*) and disruptions to very long chain fatty acid oxidation (9, 10, 55, 56). *Abcd1* knockout mice challenged with cuprizone and MOG-immunization exhibited altered neuroinflammatory responses that emulated adrenoleukodystrophy-related features, including blood brain barrier disruption and perivascular

infiltrates, indicating that peroxisome dysmetabolism perturbs neuroinflammatory responses (57). Our findings further indicate that cell intrinsic disruptions of peroxisomal integrity in microglia are sufficient to undermine responses to demyelination, reinforcing a critical role for microglial peroxisome metabolism in peroxisomal disorders such as adrenoleukodystrophy. However, it should be emphasized that the generalizability of our findings targeting PEX5, which undermines peroxisome biogenesis and integrity, may be limited in diseases with intact peroxisome biogenesis, including adrenoleukodystrophy, where PEX5 expression and function are conserved and where pathogenic mechanisms stem from disruptions in specific peroxisomal pathways rather than global peroxisome dysfunction.

In summary, we report that myelin debris clearance, sterol export, and lipid droplet metabolism in microglia depend on PEX5, presumably through peroxisome related mechanisms. Our findings implicate an interrelationship between microglial peroxisomes and remyelination and encourage further exploration into the mechanisms interrelating peroxisomes and remyelination promoting properties in microglia.

Methods

Sex as a biological variable

Both male and female animals were used with similar findings across both sexes.

Mouse strains and alleles

Offspring heterozygous for the *Cx3cr1*$^{\text{CreERT2-EYFP}}$ allele and homozygous for the *Pex5*$^{\text{lox}}$ allele were used for conditional knockout of PEX5 in myeloid cells, including microglia (*Cx3cr1*$^{\text{CreERT2/wt}}$, *Pex5*$^{\text{lox/lox}}$). Littermates heterozygous for *Cx3cr1*$^{\text{CreERT2-EYFP}}$ and heterozygous or non-carrier for *Pex5* $^{\text{lox}}$ (*Cx3cr1*$^{\text{CreERT2/wt}}$, *Pex5*$^{\text{lox/wt,wt/wt}}$) served as controls. To activate Cre-

mediated recombination, PEX5cKO and control mice, ages 8-12 weeks, received daily intraperitoneal injections of 2 mg tamoxifen dissolved in corn oil for five consecutive days. *Cx3cr1*$^{CreERT2\text{-}EYFP}$ mice (Stock no. 021160) and *Pex5*^{lox} mice (Stock no. 031666) were obtained from The Jackson Laboratory (Bar Harbor, ME, USA) and maintained under pathogen-free conditions at MD Anderson Cancer Center Animal Facility.

Cuprizone diet

0.2% cuprizone pellet diet (Envigo) was administered ad libitum to experimental mice for 6 weeks. Tamoxifen was administered two weeks prior to starting CPZ to enable turnover between matrix protein-intact and -deficient peroxisomes in PEX5 depleted myeloid cells.

Bone marrow derived macrophages

Bone marrow isolate was extracted from femur and tibia using high g-force centrifugation (>10,000g, 30 seconds, 4°C) and collected in a sterile 1.5 mL microcentrifuge tube. Isolate was incubated in RBC lysis buffer (Biolegend) on ice for 5 minutes followed by quenching with 10 volumes of ice-cold culture medium. Isolate was filtered through a 70-micron strainer, centrifuged at 500 g for 10 minutes at 4°C, resuspended in culture medium, and live cells counted using trypan blue. Isolate was seeded at a concentration of 1.0-2.0 x 10^5 live cells per mL in culture medium and cultured for 7 days for macrophage differentiation. Culture medium was replaced with fresh medium every 2-3 days, and consisted of 75% volume of L-glutamine-enriched RPMI1640 medium, 10% fetal bovine serum, and 15% L929 conditioned medium, with 100 U/mL of penicillin-streptomycin. To deplete PEX5 in vitro, medium was supplemented with 1.0 μM of 4-hydroxytamoxifen (Sigma H7904) throughout the 7-day differentiation and during experimental assays for both PEX5cKO and control macrophages. 4-hydroxytamoxifen stock solution was dissolved in 100% ethanol to 15 mM and added directly to culture medium at 1:15,000 dilution

(final concentration of 1.0 μM). Fresh 4-hydroxytamoxifen was added when replacing culture medium every 2-3 days.

L929 conditioned medium

L929 cells (mouse fibroblast cell line, ATCC CCL-1) with low passage number (P<10) were plated in T175 flasks at a split ratio of 1:10 in DMEM medium with 10% fetal bovine serum and 100 U/mL of penicillin-streptomycin. After 8 days, conditioned medium was harvested and sterile filtered using 0.22-micron filter and stored at -80°C. After thawing, conditioned medium was immediately used or stored in 4 °C for no longer than 2 weeks.

Immunofluorescence

For formalin-fixed formaldehyde embedded sections, anesthetized mice were transcardially perfused with 40 mL of 4.0% paraformaldehyde in PBS. Mouse brain was postfixed in 10% buffered formalin for minimum 48 hours at room temperature on a rocker. Formalin fixed brains were dehydrated and embedded in paraffin and sectioned at 5μm thickness onto pre-treated glass slides. Sections were rehydrated and subjected to heat-mediated antigen retrieval in acidic citrate buffer with 0.05% Tween20. Sections were blocked with blocking buffer (3% bovine serum albumin, 1% horse serum in TBS with 0.1% Tween20) for 1 hour and incubated with primary antibodies in blocking buffer overnight at 4ºC. After washing in TBS, sections were incubated with fluorophore-conjugated secondary antibodies diluted 1:1,000 in blocking buffer for 1 hour at room temperature protected from light. Slides were incubated with Hoescht 33342 (Invitrogen, H1399) in TBS for 10 minutes and then washed in TBS. No.1.5 coverslips were mounted with glycerol-based, anti-fade mounting solution (Invitrogen, 36980) and cured at room temperature protected from light.

For frozen sections, anesthetized mice were transcardially perfused with 40 mL of 4.0% paraformaldehyde in PBS. Mouse brain was postfixed in ice cold 4.0% paraformaldehyde in PBS overnight (~12 hours) at 4ºC on a rocker. Fixed brains were cryoprotected by incubating in hyperosmolar sucrose solution (30% sucrose in PBS) at 4ºC for 2-3 days. Brains were embedded in OCT compound and stored at -80ºC. OCT-embedded brain tissue was cryo-sectioned into 7µm thick sections placed on pre-treated glass slides. Sections were rinsed with TBS and permeabilized using 1.0% Triton-X100 in TBS overnight at 4ºC. Following permeabilization, sections were blocked with blocking buffer (3% bovine serum albumin, 1% horse serum in TBS with 0.1% Tween20) for 1 hour and incubated with primary antibodies in blocking buffer overnight at 4 ºC. After washing in TBS, sections were incubated with fluorophore-conjugated secondary antibodies diluted 1:1,000 in blocking buffer for 1 hour at room temperature protected from light. Slides were incubated with Hoescht 33342 (Invitrogen, H1399) in TBS for 10 minutes and then washed in TBS. No.1.5 coverslips were mounted with glycerol-based, anti-fade mounting solution (Invitrogen, 36980) and cured at room temperature protected from light.

Primary antibodies included SOX10 (goat, R&D Systems, AF2864), ASPA (rabbit, EMD Millipore, ABN1698), MBP (mouse, Biolegend, 808401), GAL3 (rat, Biolegend, 125402), LAMP1 (rabbit, Abcam, ab24170), PDGFRα (rabbit, R&D Systems, AF1062), and SYP (rabbit, Abcam, ab32127), IBA1 (rabbit, Fujifilm Wako, 019-19741; goat, Fujifilm Wako, 011-27991), and dMBP (rabbit, Sigma-Aldrich, AB5864).

Immunocytochemistry

Bone marrow isolate was cultured on glass coverslips within 6-well plates. Following macrophage differentiation, coverslips were washed with DPBS and immediately fixed using 4.0% paraformaldehyde for 10 minutes at room temperature followed by a second DPBS wash. For

permeabilization, coverslips were incubated with 0.1% Triton-X100 in D-PBS for 15 minutes at room temperature followed by a DPBS wash. Coverslips were blocked with blocking buffer (3% bovine serum albumin, 1% horse serum in TBS with 0.1% Tween20) for 1 hour and incubated with primary antibodies in blocking buffer overnight at 4ºC. After washing in TBS, coverslips were incubated with fluorophore-conjugated secondary antibodies diluted 1:1,000 in blocking buffer for 1 hour at room temperature protected from light, followed by incubation with Hoescht 33342 (Invitrogen, H1399) in TBS for 10 minutes and a final wash in TBS. Coverslips were inverted onto pre-treated slides with glycerol-based, anti-fade mounting solution (Invitrogen, 36980) and cured at room temperature protected from light.

Lipid staining

Whole brains were fixed, cryoprotected, OCT-embedded, and frozen per above. After cryosectioning, 7µm thick sections were incubated in open air at room temperature for 30 minutes followed by three TBS washes, 10 minutes each. Cryosections were then incubated with 1.0 µM of BODIPY 493/503 (Invitrogen, D3922), 5.0 µg/mL of DyLight649-conjugated Griffonia Simplicifolia Lectin I, Isolectin B4 (Vector Laboratories, DL-1208), and propidium iodide (1:1000) in TBS for 30 minutes at room temperature and protected from light. After washing sections with TBS, No.1.5 coverslips were mounted using glycerol-based, anti-fade mounting solution (Invitrogen, 36980). Mounted slides were cured at room temperature protected from light and stored at -20C.

Immunoblotting

Plated bone marrow-derived macrophages were washed twice with sterile DPBS and directly lysed using ice-cold RIPA lysis buffer (ThermoFisher, 89900) supplemented with protease inhibitor cocktail (Roche, 11836170001, 1 tablet per 10 mL of RIPA) and phosphatase inhibitor solution

(Sigma, P5726, 1:100 dilution in RIPA). Following sonication and centrifugation at >10,000 g for 15 minutes at 4°C, cleared supernatant was stored at -80°C. LDS sample buffer (Invitrogen, NP0007) was added to 1x concentration and dithiothreitol (DTT, Roche 10197777001) was added to 50 mM concentration. Samples were heated to 95°C for 5 minutes and loaded onto precast tris-bis polyacrylamide gels for electrophoresis. Proteins were transferred onto nitrocellulose membranes via rapid semi-dry protein transfer. Membrane was blocked in 5% non-fat milk in TBS with 0.1% Tween20 (TBST) for 1 hour at room temperature. Blot was incubated with primary antibodies diluted 1:500-1000 in TBST with 3% BSA overnight at 4°C. After washing with TBST, blots were incubated with HRP-conjugated secondaries in TBST with 5% non-fat milk for 1 hour at room temperature and followed with a second wash in TBST. Blots were incubated with chemiluminescent substrate (ThermoFisher, 34577) and images acquired using X-ray films. Primary antibodies included PEX5 (rabbit, Proteintech, 12545-1-1AP), and β-actin (mouse, Sigma-Aldrich).

RNA purification from bone marrow-derived macrophages

Plated bone marrow-derived macrophages were washed with sterile DPBS twice and directly lysed with RLT lysis buffer (Qiagen, 79216) supplemented with 2-mercaptoethanol (1:100 dilution). Lysate was stored at -80°C until downstream RNA extraction. For RNA extraction, frozen lysate was thawed and then homogenized using QIAshredder columns (Qiagen, 79656) per manufacturer's instructions. Following homogenization, RNA was purified using the Qiagen RNeasy mini columns (Qiagen, 74106) with DNA on-column digestion included using RNase-free DNase I (Qiagen, 79254) per manufacturer's instructions. Total RNA was eluted in nuclease free water and stored at -80°C.

RTqPCR for bone marrow-derived macrophages

Purified total RNA was reverse transcribed into cDNA using iScript reverse transcriptase (Bio-Rad, 1708841) per manufacturer's instructions. Real time qPCR was performed using the iTaq polymerase, universal SYBR green system (Bio-Rad, 1708841) on an Applied Biosytems^{TM} 7500 Real Time PCR system per manufacturer's instructions.

Bulk RNA sequencing for bone marrow-derived macrophages

Purified total RNA with an RNA integrity number (RIN) above 7.0 were submitted to Novogene Inc. for library preparation and next-generation sequencing. mRNA was enriched and cDNA libraries were generated from total RNA using the NEBNext Ultra II RNA library prep kit (New England Biolabs) per manufacturer's instructions. cDNA libraries were pooled and sequenced on the NovaSeq 6000 to attain $20x10^6$ paired reads of 150 bases per read (20M, PE150, 6 Gb). Raw reads were recorded into FASTQ files and were filtered for clean reads by removing (a) adapter-containing reads, (b) low quality reads having more than 50% bases with a Qscore $\leq$5, and (c) reads composed of >10% undetermined bases.

Bulk RNA sequencing data processing and analysis

Paired reads were aligned to the GRCm38 reference genome using graph-based alignment (HISAT2, v2.1.0) (58). Aligned sequences were assembled into transcripts using the StringTie algorithm (StringTie, v2.2.1) (59). Coverage values generated per transcript were converted into hypothetical gene counts using the formula of gene counts = coverage x (transcript length/read length). Raw gene counts were transformed using variance stabilizing transformation followed by dimensionality reduction using principal component analysis to assess for batch effects and visualize patterns in low dimensional space. Raw gene count were then inputted into the DESeq pipeline for normalization and DEG analysis (DESeq2, v1.46.0) (60).

Myelin debris isolation and challenge

589 Whole brains were excised from adult wild-type C57BL6 male mice and minced with a scalpel in
590 ice-cold 0.32 M sucrose buffer (0.32 M sucrose, 20 mM Tris-HCl, 2 mM Na_2EDTA, pH 7.45)
591 supplemented with protease inhibitors (Roche, 11836170001). Minced brains were homogenized
592 in 0.32 M sucrose buffer using a pre-cooled Tenbroeck tissue grinder (Pyrex, No. 7727-07) on ice
593 until achieving a smooth, milky homogenate. Homogenate was divided between six ultra-
594 centrifuge tubes, wherein 13 mL of homogenate was gently layered onto 17 mL of ice-cold 0.83
595 M sucrose buffer (0.83 M sucrose, 20 mM Tris-HCl, 2 mM Na_2EDTA, pH 7.45) per tube, with
596 care taken to avoid mixing between layers. The sucrose gradient was centrifuge at 25,000 RPM
597 for 1.5 hours at 4°C. The resulting intermediate layer was recovered and re-homogenized using 10
598 strokes in a pre-cooled Tenbroeck tissue grinder on ice. Crude myelin was diluted in ice-cold
599 hypotonic Tris-HCl buffer (20 mM Tris-HCl, 2 mM Na_2EDTA, pH 7.45) and centrifuged at 17,000
600 RPM for 15 minutes at 4°C. After decanting supernatant, crude myelin was resuspended in Tris-
601 HCl buffer and pelleted at 17,000 RPM for 15 minutes at 4°C. To enhance myelin purity, crude
602 myelin was resuspended in 0.32 M sucrose buffer and submitted to a second sucrose gradient
603 centrifugation followed by two repeated osmotic shocks in hypotonic Tris-HCl buffer as described
604 above. After the last osmotic shock step, myelin debris was resuspended in ice-cold sterile D-PBS
605 and transferred to pre-weighted 1.5 mL microtubes. Myelin debris was pelleted at 22,000 g for 10
606 minutes at 4°C and weighted and then resuspended in sterile DPBS to a stock concentration of 200
607 mg/mL and stored at -80°C. 10 to 12 adult mice were used per batch of purified myelin. For myelin
608 debris challenge, myelin debris was thawed and homogenized by passing five times through a
609 sterile 30G needle. Myelin debris was added to the culture medium to a concentration of 0.50
610 mg/mL for durations indicated in the study.

611 **Transmission electron microscopy**

612 Anesthetized mice were transcardially perfused with 40 mL of 4.0% paraformaldehyde in PBS.
613 Mouse brains were hemisected and incubated in EM fixative solution (2.5% EM-grade
614 glutaraldehyde and 2% EM-grade paraformaldehyde in 0.1 M cacodylate solution buffered to 7.4
615 pH) at 4°C for minimum 3 days on a rocker. A 1-mm thick coronal section was then taken from
616 the coronal plane containing dorsal hippocampus (Bregma -1.2mm to -2.2mm), which plane
617 includes corpus callosum area most affected by 0.2% cuprizone diet. Tissue was resected to
618 achieve a section area of 1.0 mm^2 and submitted to the High Resolution Electron Microscopy
619 Facility at MD Anderson for processing and imaging. Samples were washed in 0.1 M sodium
620 cacodylate buffer, treated with 0.1% Millipore-filtered cacodylate buffered tannic acid, postfixed
621 with 1% buffered osmium tetroxide, and stained en bloc with 1% Millipore-filtered uranyl acetate.
622 Samples were dehydrated in increasing concentrations of ethanol, infiltrated, and embedded in
623 LX-112 medium. Samples were polymerized in a 60°C oven for approximately 3 days. Ultrathin
624 sections were cut in a Leica Ultracut microtome (Leica, Deerfield, IL), placed on formvar coated
625 single slot copper grids, stained with uranyl acetate and lead citrate, and examined in a JEM 1010
626 transmission electron microscope (JEOL, USA, Inc., Peabody, MA) at an accelerating voltage of
627 80 kV. Digital images were obtained using AMT Imaging System (Advanced Microscopy
628 Techniques Corp, Danvers, MA).

629 **Confocal microscopy and image processing**

630 Confocal imaging was performed using a Leica TCS SP8 laser scanning confocal microscope
631 equipped with an acuosto-optical beam splitter (AOBS). Multiprobe fluorescence imaging with z-
632 stacking was performed through sequential bidirectional scanning using between-lines acquisition
633 mode, 600 Hz scan speed, 3000x3000 format, and optimized z-step sizes. For crystals imaging, a
634 separate channel was configured for reflection microscopy and scanned sequentially with

fluorescence acquisition channels. The reflection imaging channel used a PMT detector, with the AOBS configured to Reflection mode. An 458nm argon laser was used for incident light, and detection wavelength range was optimized to 455-463nm. Image z stacks were projected onto 2D composite images using maximum intensity projection method. Image processing and quantification were conducted using ImageJ software. Acquired images were converted to 8-bit grey scale and background noise mitigated using a median filter with pixel radius of 2.0. For particle analysis and counting, images were segmented via thresholding and converted to binary. Cells counts were obtained via nuclei quantification within segmented cell masks.

Brain nuclei isolation

Anesthetized mice were transcardially perfused with 40 mL of PBS. After perfusion, an 8-12 mm^3 sample of brain tissue containing corpus callosum adjacent was excised and minced into ~1 mm^3 pieces on wet ice per mouse. Minced tissue was transferred to pre-chilled glass Dounce homogenizers with homogenization buffer comprised of 250 mM sucrose, 25 mM KCl, 5 mM $MgCl_2$, 1.0 µM DTT, and 0.1% TritonX100 in 10 mM Tris buffer, pH 8.0, supplemented with RNase (0.4 U/µL RNasin® Promega and 0.2 U/µL SUPERaseIn™ Invitrogen) and protease (1x cOmplete™ cocktail Roche) inhibitors and nuclei acid dyes (1.0 µg/mL PI and 1.0 µg/mL DAPI). Tissue was homogenized on wet ice using a loose-fitting pestle for 5 strokes followed by a tight-fitting pestle for 15 strokes. Homogenate was filtered through 50-µm strainers into low DNA binding microtubes. Nuclei were pelleted at 400 g, 4°C, for 5 minutes and resuspended in isolation buffer consisting of 1 mg/mL of BSA in nuclease free DPBS supplemented with RNase (0.4 U/µL RNasin® Promega and 0.2 U/µL SUPERaseIn™ Invitrogen) and protease (1x cOmplete™ cocktail Roche) inhibitors and nuclei acid dyes (1.0 µg/mL PI and 1.0 µg/mL DAPI). Nuclei were filtered through a 40-µm strainer and isolated from debris via fluorescence activated nuclei sorting

using singlet and $DAPI^+$, PI^+ dual gating, achieving an estimated nuclei concentration of 900 to 1000 nuclei/μL.

Single nuclei RNA sequencing

Single nuclei RNA sequencing libraries were constructed in tandem using the 10x Genomics Chromium Single Cell 3' system (v3.1, dual index) per manufacturer's instructions. Dual indexed libraries were sequenced using NovaSeq 6000 (Illumina) with 150 bp paired end sequencing at a target depth of 35,000 reads per nucleus and target sample size of 9000 nuclei per library. Demultiplexed raw reads were filtered and aligned to the reference genome (mm10) using cellranger count with intron reads included (10x Genomics Cell Ranger, v7.0.0) (61). Per library, ambient RNA contamination was scrubbed using decontX (celda, v1.22.1) (62). Low quality transcriptomes were filtered out using gene count and mitochondrial read cutoffs of 200 and 5.0%, respectively. Genes detected in fewer than 10 cells were excluded from analysis. Gene counts were then normalized and scaled using the Seurat LogNormalize method followed by scaling (Seurat, v5.2.1) (63). Dimensionality reduction and cell clustering were achieved using principal component analysis (PCA) and the Seurat shared nearest neighbor (SNN) clustering algorithm, respectively (Seurat, v5.2.1) (63). Doublets were detected for each dataset individually via scDblFinder (scDblFinder, v1.20.2) using an estimated doublet rate of 1.0% per 1000 nuclei detected (64). After excluding doublets, processed datasets were aggregated into a single library. Normalization, dimensionality reduction, and clustering were repeated for the aggregated library using SCTransform (65), PCA, and Seurat SNN clustering algorithm, respectively (Seurat, v5.2.1) (63). Differentially expressed genes per cluster were identified via the Wilcoxon Rank Sum test using FindAllMarkers (Seurat, v5.2.1), with $\log_2$ fold change and percent expressed thresholds of 0.25 and 25%, respectively. For pseudobulk analysis, a matrix of gene counts across samples was

generated by summing the corrected UMI counts per gene across all cluster-annotated cells per sample. DEG analysis was performed on the generated gene count matrices using DESeq (DESeq2, v1.46.0) (60).

Pathway analysis

KEGG (Kyoto Encyclopedia of Genes and Genomes) pathway analysis was performed via overrepresentation analysis with one-sided Fisher's exact test using enrichKEGG (clusterProfiler, v4.14.6) (66). Overrepresentation analysis was performed using upregulated (p. adj <0.01, $\log_2$ fold change > 0.25) and downregulated (p. adj <0.01, $\log_2$ fold change < -0.25) DEGs to determine enriched and reduced pathways, respectively. Background genes used in pathway analysis between DMAM2, DMAM1, and DMAM0 clusters required minimum average expression of 0.5 within the DMAM0 cluster. Background genes used in bulk RNA sequencing pathway analysis required minimum average expression of 10 across libraries. Minimum and maximum cutoffs for pathway sizes were 10 and 300, respectively. For bulk RNA sequencing, upstream regulator activity was inferred from DESeq analysis-derived fold change using Qiagen IPA suite (67). Thresholds for statistically significant changes in upstream regulator activity included adjusted p value and z-score cutoffs of 0.05 and |2.0|, respectively.

Enrichment analysis of customized gene sets in bone marrow-derived macrophages

Customized gene sets were generated using annotated microglial cluster marker genes from published single nuclei RNA sequencing datasets (68, 69). Gene sets were generated by selecting up to 100 top marker genes (ranked by p) corresponding to annotated clusters. Enrichment of gene sets in PEX5cKO relative to control was assessed through gene set enrichment analysis using clusterProfiler (v4.14.6) and gene lists ranked by fold change. An adjusted p value of 0.05 served

as a cutoff for statistically enriched (normalized enrichment score > 0) or decreased (normalized enrichment score < 0) gene sets in PEX5cKO relative to control.

Trajectory analysis

Developmental trajectories were inferred using slingshot (slingshot, v 2.14.0) (17). Low-dimensional space coordinates from uniform manifold approximation and projection and cluster annotations were inputted into slingshot to map connections between adjacent clusters using a minimum spanning tree and to infer lineages across mapped connections. The initial clusters within microglial and oligodendrocyte lineages were specified based on prior knowledge using established gene markers for homeostatic microglia and committed oligodendrocyte precursors, respectively. Smooth lineage curves were generated using a resolution of up to 400 cells.

Statistics

Statistical analysis was conducted in R. Unpaired, two-tailed t test was used for comparisons between two groups. FDR method was used for multiple testing correction. For comparison between multiple groups, one-way ANOVA was conducted followed by Tukey HSD for post-hoc testing. A *P* value less than 0.05 was considered significant. Number of animals or wells used per experiment are indicated in the corresponding figures. For immunoblotting and RT-qPCR, representative data from multiple independent replicates are shown. No statistical methods were used to predetermine sample size. No blinding or randomization was implemented during experiments.

Study approval

Mouse work was conducted in accordance with protocols approved by the Institutional Animal Care and Use Committee of the University of Texas MD Anderson Cancer Center.

Data availability

Underlying data for the figures presented in the main text and supplemental material are available within the Supporting Data Values file. Raw and processed data for bone marrow-derived macrophage bulk RNA sequencing and mouse brain single cell RNA sequencing are available on the Gene Expression Omnibus repository within the GSE255159 and GSE272138 series, respectively. The analytic code used for RNA-seq analysis is publicly available on GitHub at https://github.com/loui-kwam/PEX5 (GitHub ID: loui-kwam).

Author contributions

JABV contributed to study conception and design, optimization and conduction of experiments, data analysis and interpretation, and manuscript drafting and editing. YLPS assisted and performed immunofluorescence sample prep and immunoblotting. KAS assisted and performed immunofluorescence sample prep, image acquisition, and analysis. YG and XZ assisted with animal husbandry and provided support during experiments. JH contributed to study conception and design, data interpretation, and manuscript editing.

Acknowledgements

This work was supported by the NIH through F31NS124110 and R01NS127933 grants. We would like to thank the editorial support provided by Sarah J. Bronson, Scientific Editor at the MD Anderson Cancer Center Research Medical Library. We acknowledge the cancer center support grant (CCSG) NIH P30CA016672 and thank Kenneth Dunner Jr. at the High Resolution Electron Microscopy Facility for assistance with transmission electron microscopy sample prep and imaging. We also extend our gratitude to the Research Animal Support Facility at Houston and MDACC Veterinary Medicine and Surgery department for their support related to animal husbandry and veterinary care.

References

1. Lodhi IJ, and Semenkovich CF. Peroxisomes: a nexus for lipid metabolism and cellular signaling. *Cell Metab.* 2014;19(3):380-92.
2. Di Cara F, et al. The peroxisome: an up-and-coming organelle in immunometabolism. *Trends Cell Biol.* 2023;33(1):70-86.
3. Di Cara F, et al. Peroxisome-Mediated Metabolism Is Required for Immune Response to Microbial Infection. *Immunity.* 2017;47(1):93-106 e7.
4. Nath AS, et al. Modulation of the cell membrane lipid milieu by peroxisomal beta-oxidation induces Rho1 signaling to trigger inflammatory responses. *Cell Rep.* 2022;38(9):110433.
5. Zimmermann JA, et al. Functional multi-organelle units control inflammatory lipid metabolism of macrophages. *Nat Cell Biol.* 2024;26(8):1261-73.
6. Beckers L, et al. Microglia lacking a peroxisomal beta-oxidation enzyme chronically alter their inflammatory profile without evoking neuronal and behavioral deficits. *J Neuroinflammation.* 2019;16(1):61.
7. Verheijden S, et al. Identification of a chronic non-neurodegenerative microglia activation state in a mouse model of peroxisomal beta-oxidation deficiency. *Glia.* 2015;63(9):1606-20.
8. Lloyd AF, and Miron VE. The pro-remyelination properties of microglia in the central nervous system. *Nat Rev Neurol.* 2019;15(8):447-58.
9. Eichler FS, et al. Is microglial apoptosis an early pathogenic change in cerebral X-linked adrenoleukodystrophy? *Ann Neurol.* 2008;63(6):729-42.

10. Bergner CG, et al. Microglia damage precedes major myelin breakdown in X-linked adrenoleukodystrophy and metachromatic leukodystrophy. *Glia.* 2019;67(6):1196-209.
11. Sahasrabuddhe V, and Ghosh HS. Cx3Cr1-Cre induction leads to microglial activation and IFN-1 signaling caused by DNA damage in early postnatal brain. *Cell Rep.* 2022;38(3):110252.
12. Baes M, et al. Generation of Pex5-loxP mice allowing the conditional elimination of peroxisomes. *Genesis.* 2002;32(2):177-8.
13. Santos MJ, et al. Peroxisomal membrane ghosts in Zellweger syndrome--aberrant organelle assembly. *Science.* 1988;239(4847):1536-8.
14. Huybrechts SJ, et al. Peroxisome dynamics in cultured mammalian cells. *Traffic.* 2009;10(11):1722-33.
15. Zirngibl M, et al. Oligodendrocyte death and myelin loss in the cuprizone model: an updated overview of the intrinsic and extrinsic causes of cuprizone demyelination. *Mol Neurodegener.* 2022;17(1):34.
16. Butovsky O, and Weiner HL. Microglial signatures and their role in health and disease. *Nat Rev Neurosci.* 2018;19(10):622-35.
17. Street K, et al. Slingshot: cell lineage and pseudotime inference for single-cell transcriptomics. *BMC Genomics.* 2018;19(1):477.
18. Grajchen E, Hendriks JJA, and Bogie JFJ. The physiology of foamy phagocytes in multiple sclerosis. *Acta Neuropathol Commun.* 2018;6(1):124.
19. Cantuti-Castelvetri L, et al. Defective cholesterol clearance limits remyelination in the aged central nervous system. *Science.* 2018;359(6376):684-8.

20. Loving BA, and Bruce KD. Lipid and Lipoprotein Metabolism in Microglia. *Front Physiol.* 2020;11:393.
21. Singh R, et al. Autophagy regulates lipid metabolism. *Nature.* 2009;458(7242):1131-5.
22. Zechner R, Madeo F, and Kratky D. Cytosolic lipolysis and lipophagy: two sides of the same coin. *Nat Rev Mol Cell Biol.* 2017;18(11):671-84.
23. Chemke J, Livni N, and Rosenmann E. Adrenoleukodystrophy: evidence for cytoplasmic inclusions in white blood cells. *Pediatr Pathol.* 1986;6(2-3):173-9.
24. Ghatak NR, et al. Morphology and distribution of cytoplasmic inclusions in adrenoleukodystrophy. *J Neurol Sci.* 1981;50(3):391-8.
25. Jia J, et al. Galectin-3 Coordinates a Cellular System for Lysosomal Repair and Removal. *Dev Cell.* 2020;52(1):69-87 e8.
26. Kumar S, et al. Galectins and TRIMs directly interact and orchestrate autophagic response to endomembrane damage. *Autophagy.* 2017;13(6):1086-7.
27. Garcia-Revilla J, et al. Galectin-3, a rising star in modulating microglia activation under conditions of neurodegeneration. *Cell Death Dis.* 2022;13(7):628.
28. Aits S, et al. Sensitive detection of lysosomal membrane permeabilization by lysosomal galectin puncta assay. *Autophagy.* 2015;11(8):1408-24.
29. Dassati S, Waldner A, and Schweigreiter R. Apolipoprotein D takes center stage in the stress response of the aging and degenerative brain. *Neurobiol Aging.* 2014;35(7):1632-42.
30. Rickhag M, et al. Apolipoprotein D is elevated in oligodendrocytes in the peri-infarct region after experimental stroke: influence of enriched environment. *J Cereb Blood Flow Metab.* 2008;28(3):551-62.

31. Gudi V, et al. Synaptophysin Is a Reliable Marker for Axonal Damage. *J Neuropathol Exp Neurol.* 2017;76(2):109-25.
32. Dixit E, et al. Peroxisomes are signaling platforms for antiviral innate immunity. *Cell.* 2010;141(4):668-81.
33. van der Lienden MJC, et al. Glycoprotein Non-Metastatic Protein B: An Emerging Biomarker for Lysosomal Dysfunction in Macrophages. *Int J Mol Sci.* 2018;20(1).
34. van der Vliet D, et al. Foamy microglia link oxylipins to disease progression in multiple sclerosis. *bioRxiv.* 2024:2024.10.18.619040.
35. Deczkowska A, et al. Disease-Associated Microglia: A Universal Immune Sensor of Neurodegeneration. *Cell.* 2018;173(5):1073-81.
36. Meir KS, and Leitersdorf E. Atherosclerosis in the apolipoprotein-E-deficient mouse: a decade of progress. *Arterioscler Thromb Vasc Biol.* 2004;24(6):1006-14.
37. Wang B, and Tontonoz P. Liver X receptors in lipid signalling and membrane homeostasis. *Nat Rev Endocrinol.* 2018;14(8):452-63.
38. Berghoff SA, et al. Microglia facilitate repair of demyelinated lesions via post-squalene sterol synthesis. *Nat Neurosci.* 2021;24(1):47-60.
39. Skowyra ML, Feng P, and Rapoport TA. Towards solving the mystery of peroxisomal matrix protein import. *Trends Cell Biol.* 2024;34(5):388-405.
40. Charles KN, et al. Functional Peroxisomes Are Essential for Efficient Cholesterol Sensing and Synthesis. *Front Cell Dev Biol.* 2020;8:560266.
41. Faust PL, and Kovacs WJ. Cholesterol biosynthesis and ER stress in peroxisome deficiency. *Biochimie.* 2014;98:75-85.

42. Hogenboom S, et al. Absence of functional peroxisomes does not lead to deficiency of enzymes involved in cholesterol biosynthesis. *J Lipid Res.* 2002;43(1):90-8.
43. Hogenboom S, Wanders RJ, and Waterham HR. Cholesterol biosynthesis is not defective in peroxisome biogenesis defective fibroblasts. *Mol Genet Metab.* 2003;80(3):290-5.
44. Chu BB, et al. Cholesterol transport through lysosome-peroxisome membrane contacts. *Cell.* 2015;161(2):291-306.
45. Varsano N, et al. Two polymorphic cholesterol monohydrate crystal structures form in macrophage culture models of atherosclerosis. *Proc Natl Acad Sci U S A.* 2018;115(30):7662-9.
46. Kong J, et al. Spatiotemporal contact between peroxisomes and lipid droplets regulates fasting-induced lipolysis via PEX5. *Nat Commun.* 2020;11(1):578.
47. Kotter MR, et al. Myelin impairs CNS remyelination by inhibiting oligodendrocyte precursor cell differentiation. *J Neurosci.* 2006;26(1):328-32.
48. Lampron A, et al. Inefficient clearance of myelin debris by microglia impairs remyelinating processes. *J Exp Med.* 2015;212(4):481-95.
49. Mason JL, et al. Insulin-like growth factor (IGF) signaling through type 1 IGF receptor plays an important role in remyelination. *J Neurosci.* 2003;23(20):7710-8.
50. Pellegrino E, et al. Peroxisomal ROS control cytosolic Mycobacterium tuberculosis replication in human macrophages. *J Cell Biol.* 2023;222(12).
51. Fraldi A, et al. Lysosomal fusion and SNARE function are impaired by cholesterol accumulation in lysosomal storage disorders. *EMBO J.* 2010;29(21):3607-20.
52. Cox BE, et al. Effects of cellular cholesterol loading on macrophage foam cell lysosome acidification. *J Lipid Res.* 2007;48(5):1012-21.

53. Wu Y, et al. Microglial lysosome dysfunction contributes to white matter pathology and TDP-43 proteinopathy in GRN-associated FTD. *Cell Rep.* 2021;36(8):109581.
54. Safaiyan S, et al. Age-related myelin degradation burdens the clearance function of microglia during aging. *Nat Neurosci.* 2016;19(8):995-8.
55. Jaspers YRJ, et al. Lipidomic biomarkers in plasma correlate with disease severity in adrenoleukodystrophy. *Commun Med (Lond).* 2024;4(1):175.
56. Moser HW, Mahmood A, and Raymond GV. X-linked adrenoleukodystrophy. *Nat Clin Pract Neurol.* 2007;3(3):140-51.
57. Hashemi E, et al. A Novel Mouse Model for Cerebral Inflammatory Demyelination in X-Linked Adrenoleukodystrophy: Insights into Pathogenesis and Potential Therapeutic Targets. *Ann Neurol.* 2025;97(2):296-312.
58. Kim D, et al. Graph-based genome alignment and genotyping with HISAT2 and HISAT-genotype. *Nat Biotechnol.* 2019;37(8):907-15.
59. Pertea M, et al. Transcript-level expression analysis of RNA-seq experiments with HISAT, StringTie and Ballgown. *Nat Protoc.* 2016;11(9):1650-67.
60. Love MI, Huber W, and Anders S. Moderated estimation of fold change and dispersion for RNA-seq data with DESeq2. *Genome Biol.* 2014;15(12):550.
61. Zheng GX, et al. Massively parallel digital transcriptional profiling of single cells. *Nat Commun.* 2017;8:14049.
62. Yang S, et al. Decontamination of ambient RNA in single-cell RNA-seq with DecontX. *Genome Biol.* 2020;21(1):57.
63. Hao Y, et al. Dictionary learning for integrative, multimodal and scalable single-cell analysis. *Nat Biotechnol.* 2024;42(2):293-304.

64. Germain PL, et al. Doublet identification in single-cell sequencing data using scDblFinder. *F1000Res.* 2021;10:979.

65. Hafemeister C, and Satija R. Normalization and variance stabilization of single-cell RNA-seq data using regularized negative binomial regression. *Genome Biol.* 2019;20(1):296.

66. Yu G, et al. clusterProfiler: an R package for comparing biological themes among gene clusters. *OMICS.* 2012;16(5):284-7.

67. Kramer A, et al. Causal analysis approaches in Ingenuity Pathway Analysis. *Bioinformatics.* 2014;30(4):523-30.

68. Absinta M, et al. A lymphocyte-microglia-astrocyte axis in chronic active multiple sclerosis. *Nature.* 2021;597(7878):709-14.

69. Androvic P, et al. Spatial Transcriptomics-correlated Electron Microscopy maps transcriptional and ultrastructural responses to brain injury. *Nat Commun.* 2023;14(1):4115.

Figures

Figure 1. DMAM2 cluster emerges from PEX5cKO microglia following demyelination.

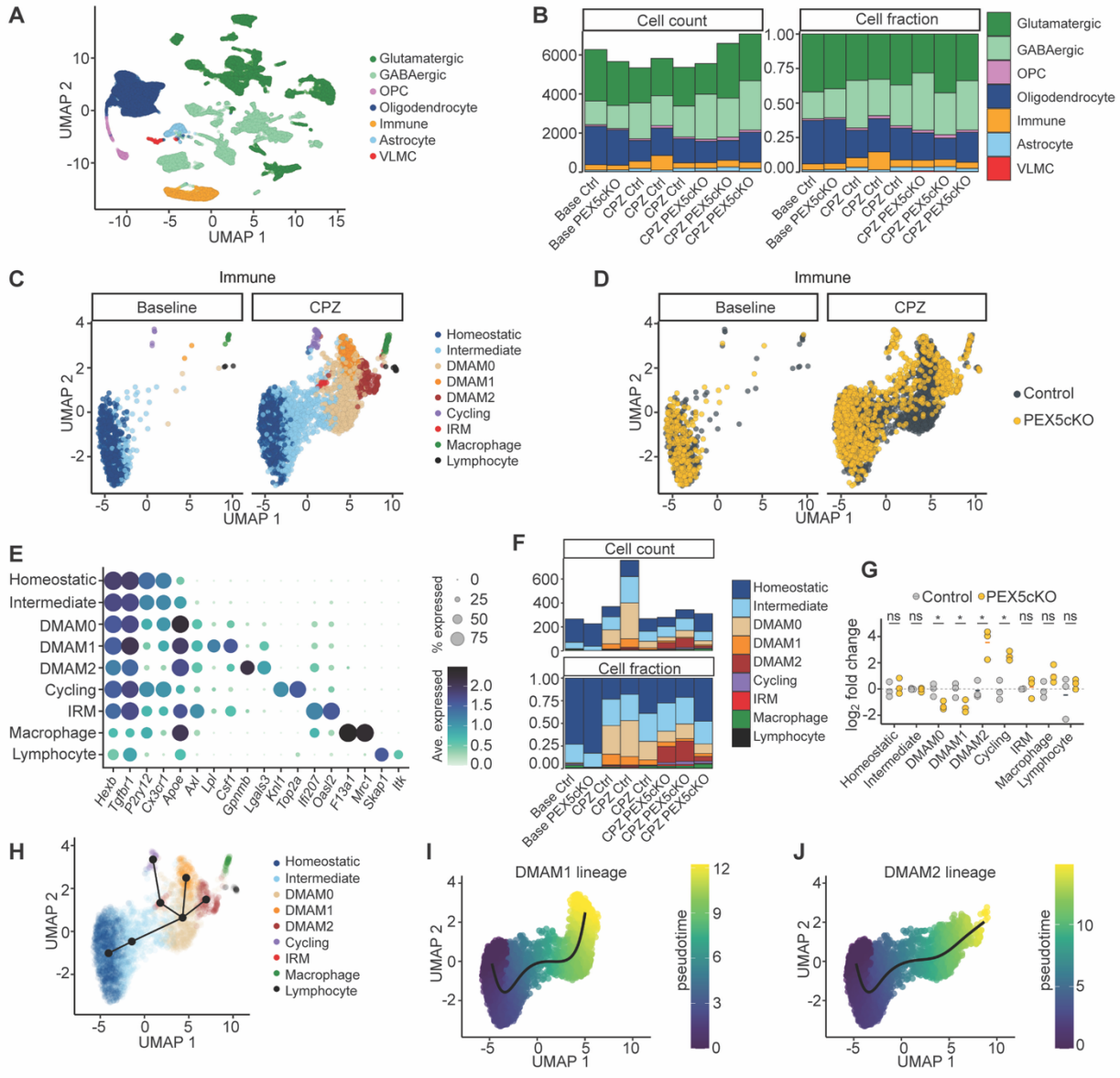

(**A**) UMAP of combined whole brain nuclei detected from baseline and CPZ conditions colored according to major cell type identity. (**B**) Cell count and cell fraction per major cell type identified within baseline and CPZ conditions across PEX5cKO and control samples. (**C**) UMAP of immune subclusters colored according to subcluster identity and split by conditions. (**D**) UMAP of immune subclusters colored according to genotype and split by condition. (**E**) Average gene expression of

marker genes per immune subcluster. Dot color and size correspond to average expression and percent expressed, respectively. (**F**) Cell count and cell fraction per immune subcluster identified within each library generated from baseline (n=1 per genotype) and CPZ (n=3 per genotype) conditions. (**G**) Cell fraction log_2 fold change relative to control per immune subcluster. Individual datapoints correspond to libraries generated from the CPZ condition. Bars correspond to the mean log_2 fold change. Unpaired, two-tailed t test, not significant (ns) $p>0.05$, * $p<0.05$. (**H**) Inferred lineages for microglial subclusters derived from slingshot analysis superimposed onto immune cell UMAP, with the Homeostatic subcluster designated as the origin cluster. (**I**) Pseudotime trajectory for DMAM1 lineage. (**J**) Pseudotime trajectory for DMAM2 lineage

UMAP, uniform manifold approximation and projection.

Figure 2. PEX5 loss impairs *Apoe* expression, aggravating lipid droplet burden and promoting lipid crystal accumulation.

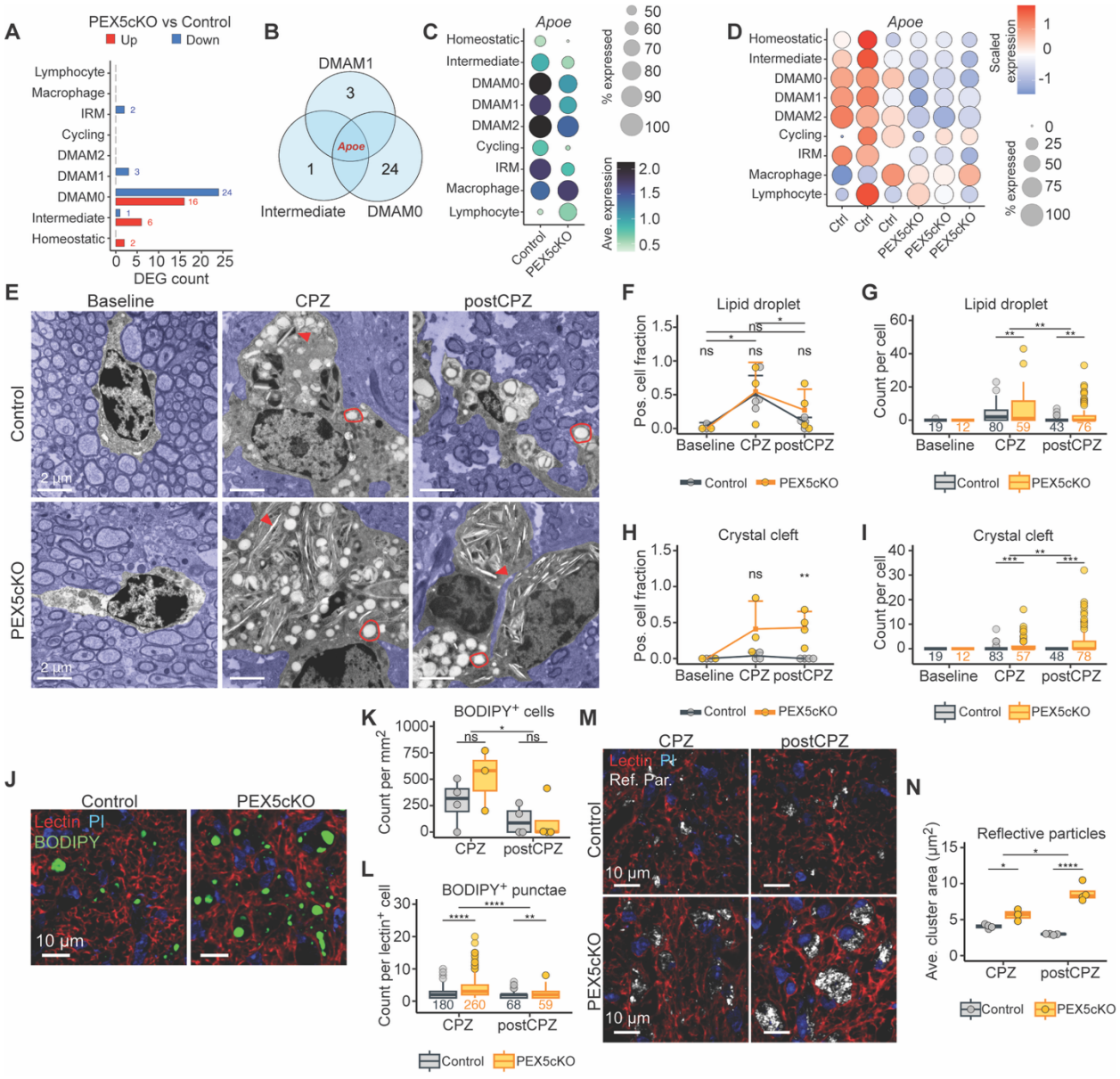

(**A**) Upregulated and downregulated pseudobulk-derived DEGs per immune subcluster. Numbers over bars indicate DEG count >0. (**B**) Venn diagram triangulating downregulated DEGs detected in DMAM0, DMAM1, and Intermediate subclusters. (**C**) *Apoe* average expression per immune subcluster split by genotype. (**D**) Per immune subcluster *Apoe* scaled expression across libraries within CPZ condition. (**E**) Representative TEM micrographs of phagocytes. Red circles and red

arrowheads mark lipid droplets and crystal clefts, respectively. Non-phagocyte area is shaded blue to ease visualization of phagocyte. Scale bar = 2.0 μm. (**F**) Lipid droplet^{+} cells as fraction of total cells imaged. (**G**) Lipid droplet count per cell assessed. (**H**) Crystal positive cells as fraction of total cells imaged. (**I**) Crystal cleft count detected per cell. (**J**) Representative micrographs for BODIPY and lectin staining within CPZ condition. Nuclei are stained with propidium iodide dye. Scale bar = 10 μm. (**K**) BODIPY^{+} cell count per mm^{2}. (**L**) BODIPY^{+} droplet count per lectin^{+} cell. (**M**) Representative micrographs of dual confocal and reflective microscopy imaging lectin stain and reflective particles. Nuclei are stained with propidium iodide. Scale bar = 10 μm. (**N**) Average area of reflective particle microclusters.

For (**E** – **N**), representative images were acquired from corpus callosum and cells analyzed and quantitated were imaged from corpus callosum. For (**F**, **H**, **K**, and **N**), individual datapoints correspond to biological replicates. For (**F** and **H**), square and error bar correspond to mean and standard deviation, respectively. For (**G**, **I**, and **L**), datapoints represent dataset outliers. Cell number assessed per group are given below each box plot. Statistical analysis for (**F – I**, **K**, **L**, and **N**) involved ANOVA followed by Tukey HSD. Not significant (ns) p.adj >0.05, *p.adj <0.05, **p.adj <0.01, ***p.adj <0.001, **** p.adj <0.0001.

Figure 3. PEX5cKO phagocytes exhibit intralysosomal crystals and cytosolic curvilinear profiles.

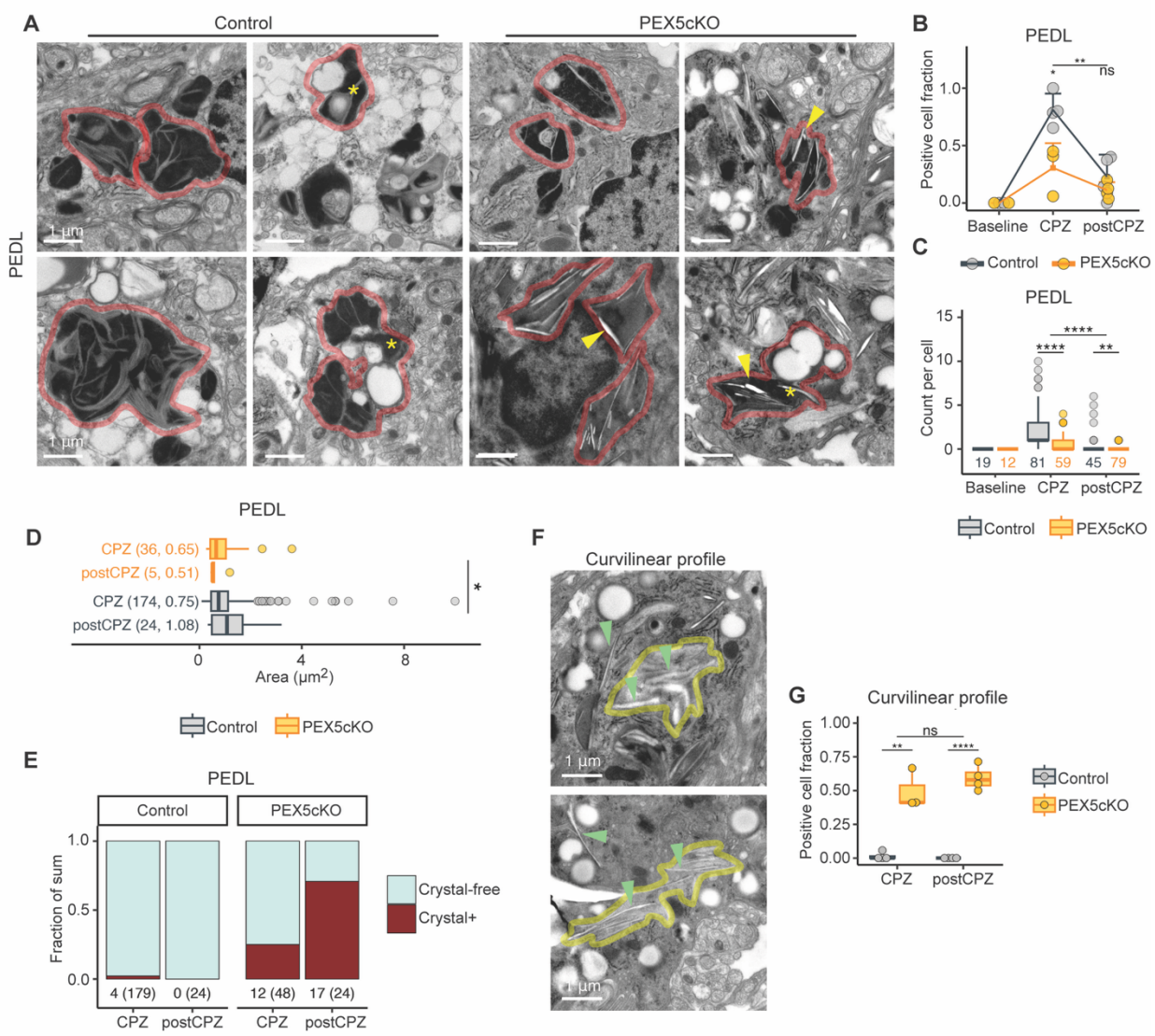

(**A**) Representative transmission electron micrographs of PEDLs indicated with a red-colored outline imaged phagocyte. Yellow asterisks mark PEDLs fusing with lipid droplets, evocative of lipophagy. Yellow arrows indicate intralysosomal crystal clefts. Scale bar = 1.0 µm. (**B**) PEDL-positive cell quantification as fraction of total cells imaged. Individual datapoints correspond to biological replicates. Square and error bar correspond to mean and standard deviation, respectively. (**C**) PEDL count per cell. Datapoints correspond to outliers and number of cells assessed are given

952 below each box plot. (**D**) Area, μm2, per crystal-free PEDL grouped by genotype and condition.
953 PEDL count and median area are indicated in parentheses. Datapoints correspond to outliers. (**E**)
954 Fraction of summed PEDLs corresponding to crystal-free and -positive PEDLs, grouped by
955 genotype and condition. Crystal-positive PEDL counts are indicated below stacked bars. Crystal-
956 free and -positive sums are indicated in parentheses. (**F**) Representative transmission electron
957 micrographs of curvilinear profiles detected in phagocytes within corpus callosum following
958 cuprizone exposure. Green arrowheads indicate representative curvilinear profiles. Yellow border
959 surrounds cluster of curvilinear profiles. Scale bars = 1.0 μm. (**G**) Curvilinear profile positive cells
960 as fraction of total cells imaged. Individual datapoints correspond to biological replicates.
961 All representative images were acquired from corpus callosum. Quantifications only used cells
962 imaged from corpus callosum. Statistical analysis for (**B**, **C**, and **G**) included ANOVA followed by
963 Tukey HSD. Not significant (ns) p.adj >0.05, *p.adj <0.05, **p.adj <0.01, **** p.adj <0.0001.
964 (**D**) Unpaired, two-tailed t test, *p <0.05
965
966

Figure 4. Exacerbated GAL3 response and lysosome turnover in PEX5cKO DMAMs.

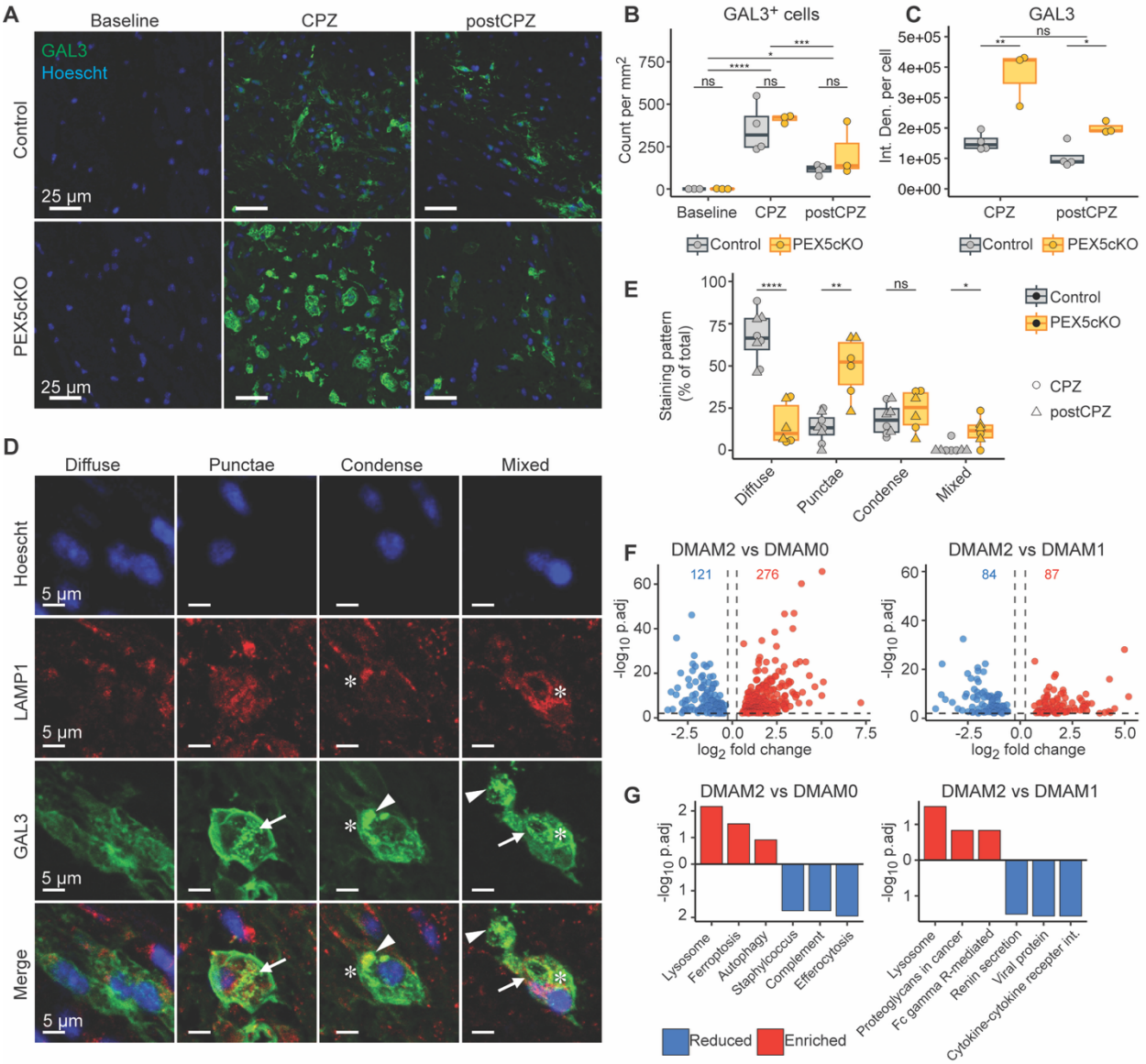

(**A**) Representative micrographs for GAL3 immunofluorescence within corpus callosum. Nuclei are stained with Hoescht dye. Scale bar = 25 µm. (**B**) GAL3$^+$ cell count per mm^2 of corpus callosum. Individual datapoints correspond to biological replicates. (**C**) Average GAL3 fluorescence integrated density per GAL3$^+$ cell. Individual datapoints correspond to biological replicates. (**D**) Representative micrographs of GAL3$^+$ cells with punctae (arrows), condensed (arrowheads), and mixed staining patterns, which frequently colocalize with LAMP1 staining

(asterisk). Scale bar = 5 μm. (**E**) Percentage of $GAL3^+$ cells subdivided by staining pattern represented in D. Individual datapoints correspond to biological replicates. Color corresponds to genotype and datapoint shape corresponds to condition. (**F**) Upregulated (red, $-\log_{10}$p.adj >2.0, $\log_2$fold change > 0.25) and downregulated (blue, $-\log_{10}$p.adj >2.0, $\log_2$fold change < -0.25) DEGs detected in the DMAM2 subcluster relative to DMAM0 (left) and DMAM1 (right) subclusters, respectively. (**G**) Top 3 enriched and reduced KEGG pathways in DMAM2 relative to DMAM0 (left) and DMAM1 (right) subclusters, respectively.

For (**A – E**), representative images were acquired from corpus callosum. Quantifications only used cells imaged from corpus callosum. Statistical analysis for (**B** and **C**) included ANOVA followed by Tukey HSD. (**E**) FDR adjusted, two tailed t test. Not significant (ns) p.adj >0.05, *p.adj <0.05, **p.adj <0.01, ***p.adj <0.001, ****p.adj <0.0001. KEGG, Kyoto Encyclopedia of Genes and Genomes

Figure 5. Oligodendrocyte density remains comparable between PEX5cKO and control genotypes across conditions.

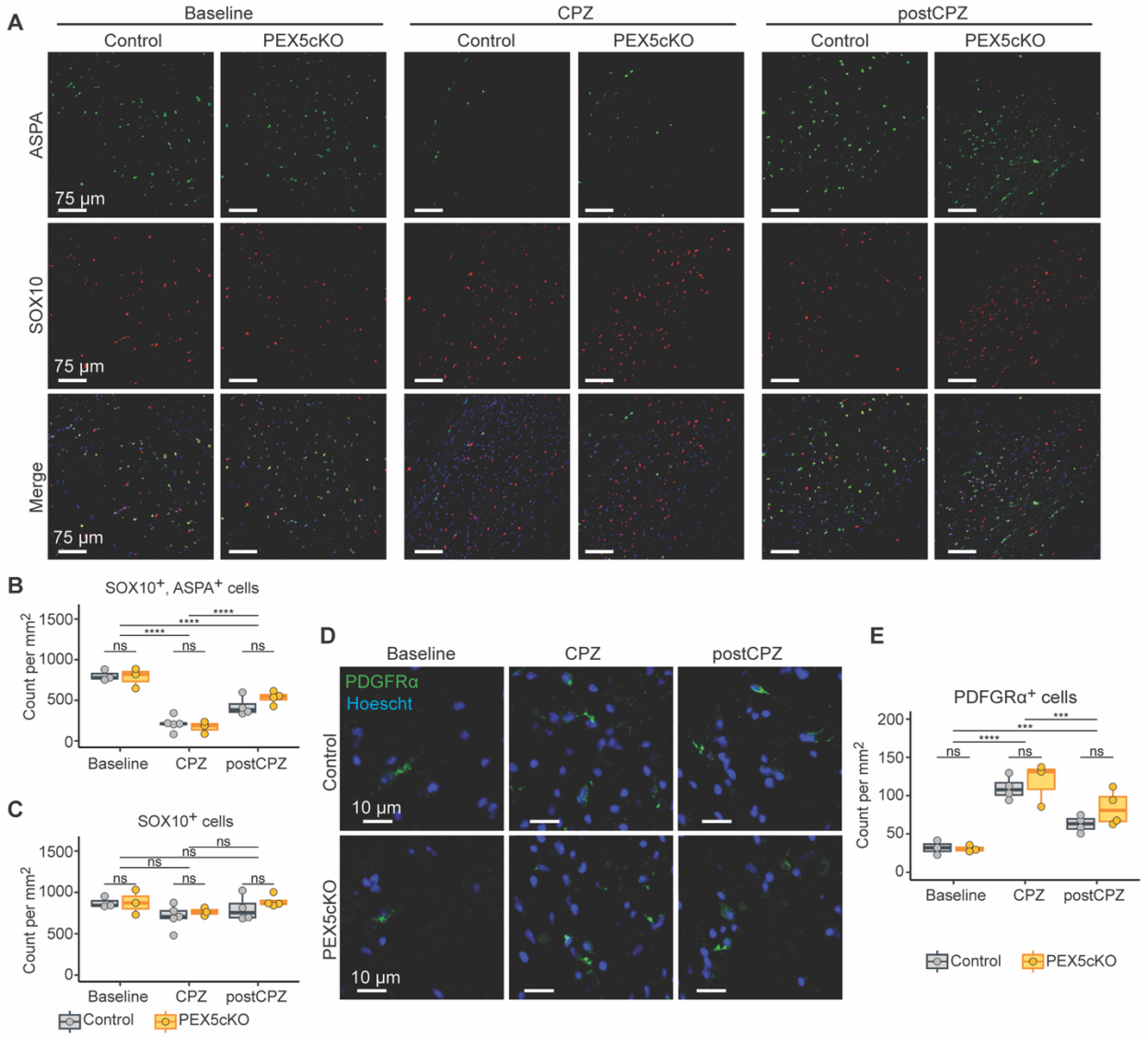

(**A**) Representative confocal micrographs for ASPA and SOX10 immunofluorescence. Nuclei are stained with Hoescht dye. Scale bar = 75 µm. (**B**) $SOX10^+$ cell count per mm^2 in corpus callosum. (**C**) $ASPA^+$, $SOX10^+$ cell count per mm^2 in corpus callosum. (**D**) Representative confocal micrographs for PDGFRα^+ immunofluorescence. Nuclei are stained with Hoescht dye. Scale bar = 10 µm. (**E**) PDGFRα^+ cell count per mm^2 in corpus callosum.

For (**A – E**), representative images were acquired from corpus callosum. Quantifications only used cells imaged from corpus callosum. Individual datapoints per box plot correspond to biological replicates. Statistical analysis for (**B**, **C**, and **E**) included ANOVA followed by Tukey HSD, ns p.adj >0.05, *** p.adj <0.001, ****p.adj <0.0001. CPZ, cuprizone-fed, postCPZ, post cuprizone removal, ns, not significant.

Figure 6. PEX5 deficiency in microglia impairs myelin debris clearance and remyelination.

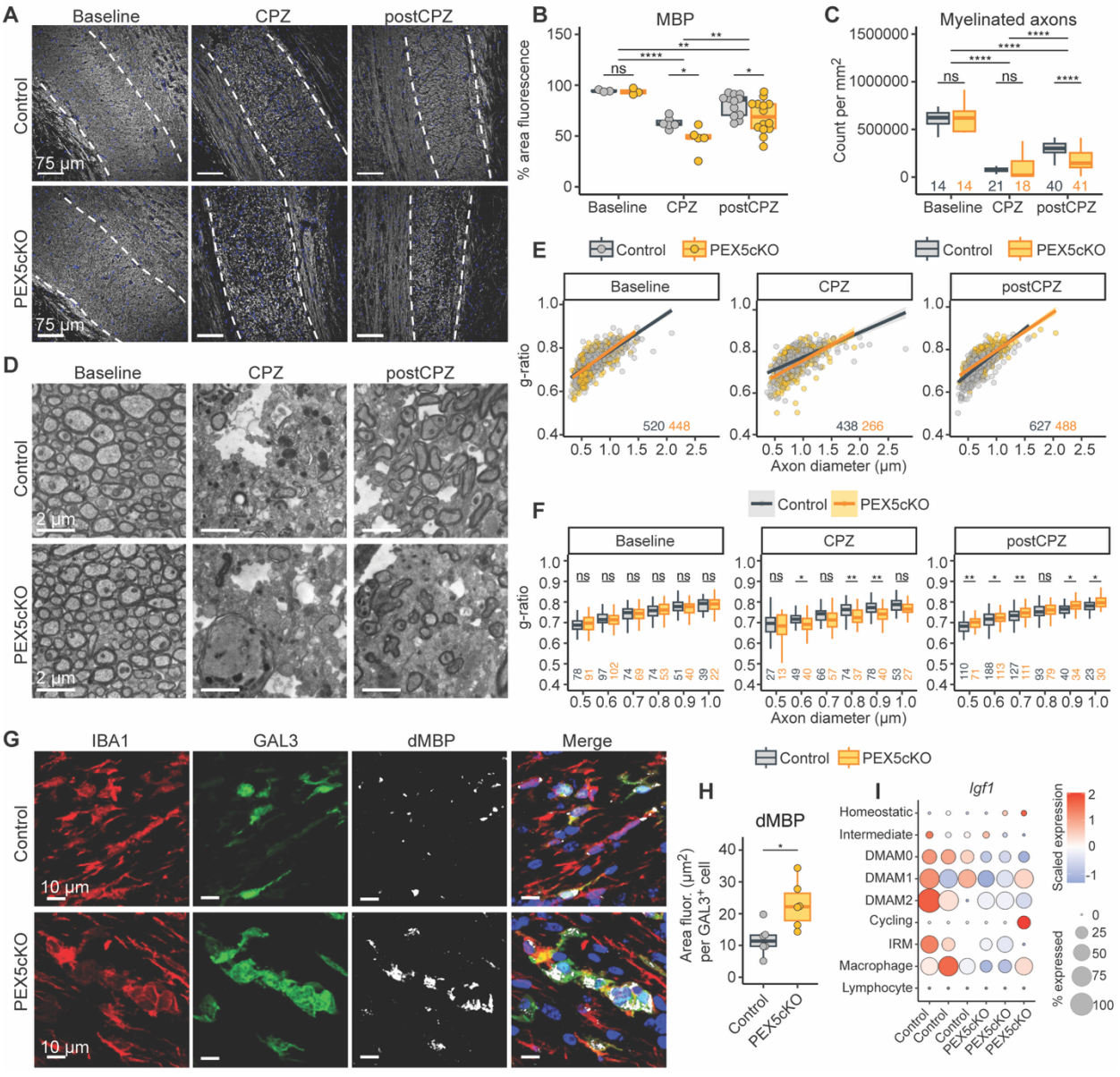

(**A**) Representative confocal micrographs for MBP immunofluorescence. Nuclei are stained with Hoescht dye. White dotted lines correspond to corpus callosum borders. Scale bars = 75 µm. (**B**) MBP^{+} percent area fluorescence. Individual datapoints correspond to biological replicates. (**C**) Myelinated axon count per mm^2 of tissue. Number of micrographs analyzed are given below each box plot. (**D**) Representative transmission electron micrographs of myelinated axons. Scale bar = 2.0 µm. (**E**) Myelinated axon g-ratio distribution across axon diameters. Lines correspond to linear

regression. Number of myelinated axons analyzed are given and colored according to genotype. (**F**) Myelinated axon g-ratio binned across axon diameters rounded to the nearest 0.1 decimal. Number of myelinated axons analyzed are given below each box plot. (**G**) Representative confocal micrographs for IBA1, GAL3, and dMBP immunofluorescence within the corpus callosum. Nuclei are stained with Hoescht dye. Scale bar = 10 μm. (**H**) $dMBP^+$ area fluorescence per $IBA1^+$, $GAL3^+$ cell assessed. Datapoints correspond to biological replicates. (**I**) Average gene expression of *Igf1* scaled across biological replicates per immune subcluster detected within the CPZ condition. Dot color and size correspond to scaled gene expression and percent expressed, respectively.

Statistical analysis for (**B**) and (**C**) included ANOVA followed by Tukey HSD comparison. (**F**) FDR adjusted, two tailed t test. Not significant (ns) p.adj >0.05, *p.adj <0.05, **p.adj <0.01, ***p.adj <0.001, ****p.adj <0.0001. (**H**) Unpaired, two tailed t test, *p <0.05.

For (**A – H**), representative images were acquired from corpus callosum. Quantifications only used cells imaged from corpus callosum. For (**C**), (**E**), and (**F**), mice used per genotype for baseline, CPZ, and postCPZ conditions were 2, 3, and 4, respectively.